Impact of optical imagery and topography data resolution on the measurement of surface fault displacement using sub-pixel image correlation

Antoine, Solène L.[1], and Liu, Zhen[1]

[1] NASA Jet Propulsion Laboratory, California Institute of Technology, Pasadena, California, USA

Corresponding author: Solène L. Antoine (solene.antoine@jpl.nasa.gov)

Key points:

- We perform a quantitative assessment of the effects of optical imagery and topography data characteristics, primarily ground resolution, on the measurement of fault surface displacements.
- Measured displacements across the fault zone are under-estimated by a factor 0.7-0.8 when using low-resolution (>10 m) compared to high-resolution (≤1 m) imagery.
- High-resolution (<0.5 m) stereo optical imagery presents as a good candidate for the future STV Earth observation system from earthquake hazard perspectives.

Abstract

The amount and spatial distribution of surface displacement that occurs during an earthquake are critical information to our understanding of the earthquake source and rupture processes. However, the earthquake surface displacement generally occurs over wide regions, includes multiple components affecting the ground surface at different spatial scales, and is challenging to characterize. In this study, we assess the sensitivity of optical imagery and topography datasets of different resolutions to the earthquake surface displacement when using optical image cross-correlation (OIC) techniques. Results show that the average noise in the output displacement maps linearly increases with decreasing image resolution, leading to greater uncertainty in determining the geometry of the faults and the associated displacement. Fault displacements are, on average, under-estimated by a factor ~0.7-0.8 when using 10 m compared to 0.5 m resolution imagery. Our analysis suggests that an optical image resolution of ≤1 m is necessary to accurately capture the complexity of the ground displacement. We also demonstrate that sub-meter vertical accuracy of the digital surface/elevation model (DSM/DEM) is also required for accurate image orthorectification, and is better achieved using high-resolution stereo optical imagery than existing global baseline topography data. Together, these results highlight the measurement needs for improving the observation of earthquake surface displacement towards the development of future Earth surface topography and topography change observing systems.

Keywords

Optical imagery, surface topography, cross-correlation, earthquake, fault, displacement

1. Introduction

Continental earthquakes often generate surface displacements that can be directly observed using satellite imagery. Measuring the amount and spatial distribution of the earthquake surface displacement then allows for untangling the shallow Fault Zone (FZ) coseismic deformation processes (Antoine et al., 2024, 2022, 2021; Barnhart et al., 2020; Li et al., 2023; Milliner et al., 2021; Zinke et al., 2019), bringing insights into the FZ mechanical behavior. Surface displacement measurements also enable constraining the earthquake rupture processes at depth using numerical inversion methods (e.g., Fialko et al., 2001; Jin and Fialko, 2021; Jolivet et al., 2014; Ragon and

Simons, 2020; Segall, 2010; Simons et al., 2002; Wang et al., 2020). However, the earthquake surface displacement can include multiple deformation components that affect the ground surface across a wide range of spatial scales. The broad scale coseismic deformation, of several tens of kilometers wide, primarily arises from the elastic response of the crust to the deep earthquake rupture (Avouac, 2015; Segall, 2010). The deformation that occurred on the faults and in their proximate vicinity, at a spatial scale of ~1-100 m, often leads to inelastic and permanent deformation of the crust which can take place through a combination of slip along primary faults, distributed deformation along secondary faults and/or fractures (e.g., DuRoss et al., 2020; Klinger et al., 2005; Rockwell et al., 2002; Teran et al., 2015; Yuan et al., 2022), and diffuse deformation of the surrounding medium (Antoine et al., 2024, 2022, 2021). The regions of surface deformation on- and near the fault correspond to what is referred to as the fault zone (FZ). Our ability to document the complete spectrum of earthquake surface deformation processes and understand the earthquake rupture process then hinges on the capability of the imaging sensors and associated processing methods to measure displacements over a wide range of spatial scales.

Observation techniques generally used to measure the earthquake surface displacement field include Synthetic Aperture Radar (i.e., Interferometric SAR, SAR pixel offsets), Global Navigation Satellite Systems (GNSS), Optical Image Correlation (OIC), and Light Detection And Ranging (LiDAR) point cloud difference. All of these techniques provide capabilities to image the ground movements with different footprints, ground resolutions, and measurement accuracies. GNSS and InSAR are the most sensitive methods with millimeter to centimeter level of accuracy, and are widely used for this purpose (e.g., Delouis et al., 2023; Floyd et al., 2020; Liu et al., 2021; Simons et al., 2002; Tong et al., 2010; Wang and Fialko, 2015). However, GNSS only permits measurements at the discrete locations, often at tens to hundreds of kilometers spacing (e.g., Fielding et al., 2020; Liu et al., 2021), and InSAR decorrelates in regions where displacement gradients are greater than the radar phase difference, which is generally along the fault ruptures (e.g., Fielding et al., 2013; He et al., 2023; Jin and Fialko, 2021; Massonnet et al., 1993; Socquet et al., 2019). For these reasons, both InSAR and GNSS present low constraints on the surface displacements that occur within and in the direct vicinity of the FZ. SAR pixel offset methods are sometimes used to retrieve the displacements closer to the faults (Jolivet et al., 2014; Liu et al., 2021; Reitman et al., 2023), but these measurements often are limited by the resolution of the publicly available SAR data which is generally about 10 m.

OIC (e.g., Aati et al., 2022; Leprince et al., 2007; Rosu et al., 2015), and differential LiDAR (e.g., Borsa and Minster, 2012; Nissen et al., 2014; Scott et al., 2018) techniques, on the other hand, allow for three-dimensional (3-D), spatially continuous, and possibly high-resolution (submeter-scale) measurement of the earthquake surface displacement field, even in regions of high-displacement gradients. Between the two techniques, OIC is more commonly used (e.g., Antoine et al., 2024, 2022, 2021; Delorme et al., 2020; Milliner et al., 2021, 2016; Teran et al., 2015; Zinke et al., 2019) as satellite optical data cover wide regions (> 15). LiDAR is generally limited to small study area because of the high-cost associated with LiDAR data acquisitions. Satellite optical imagery has been widely developed both in the public and private domains, now allowing for dense data archives in many regions of the globe. Optical imageries with different viewing angles can be combined to reconstruct the 3D ground surface (digital surface model, DSM) through photogrammetry methods, and represent a unique dataset to document the ground surface characteristics, topography, topography change, and horizonal displacement for analyzing the earthquake and FZ deformation processes. Therefore, stereo optical imaging has been proposed as one of the technology candidates for future Earth Surface Topography and Topography Change Global Observing systems such as NASA Surface Topography and Vegetation Mission (STV) (Donnellan et al., 2022, 2017).

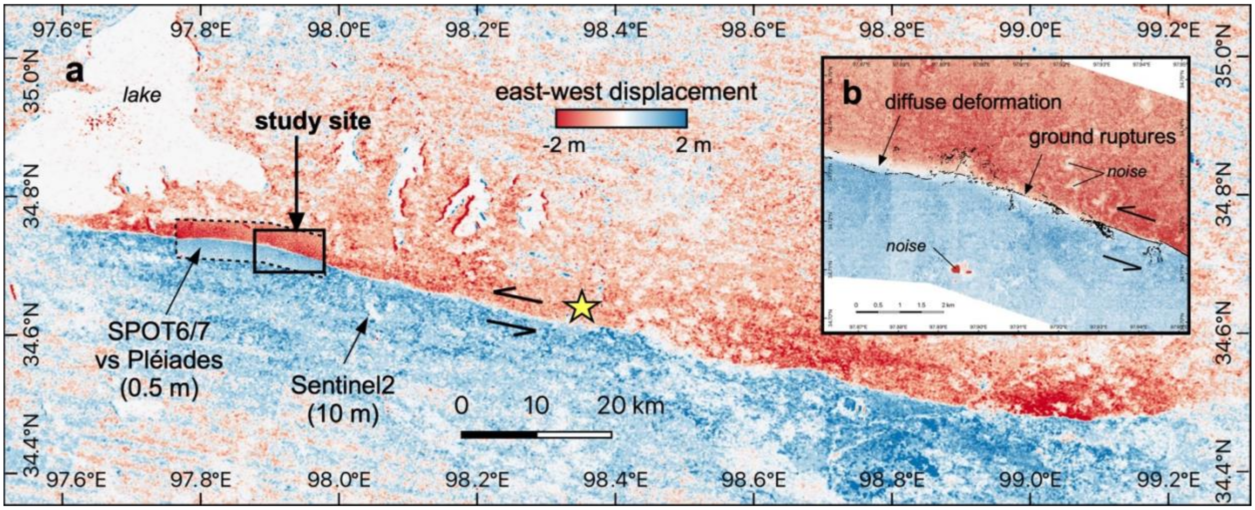

Figure 1. (a) East-west surface displacement along the 2021 Maduo, Tibet, rupture from the OIC of Sentinel-2 optical images at 10 m ground resolution (Antoine et al., 2024). HR (0.5 m) OIC result from Antoine et al. (2024), derived from the cross-correlation of SPOT6/7 and Pleiades images, and covering our study site (black rectangle) shown within the dashed black polygon. Epicenter location, from global CMT catalog (GCMT), is shown with a yellow star. (b) East-west surface displacement from the HR OIC results from Antoine (2024) across our study site. Study site area corresponds to the common area covered by all datasets, and is 8.5 km-long. Field rupture map from Yuan et al. (2022) is overlaid in black.

As of today, low-resolution (LR; 3-10 m) optical imagery (e.g., SPOT1-4, Planet, Landsat, Sentinel), because it is freely available and presents a regional/global coverage, is widely used to characterize the horizontal earthquake surface displacement field (e.g., Avouac, 2015; Chen et al., 2020; He et al., 2023; Li et al., 2022; Milliner and Donnellan, 2020; Fig. 1a). High-resolution imagery (HR; <3 m; e.g., Pleiades, WorldView, SPOT5-7) was though shown to be a more reliable source of information, especially for mapping the fault ruptures (e.g., Klinger et al., 2005; Reitman et al., 2023), and assessing the different components of the near-fault surface deformation (e.g., Antoine, 2024, 2021; Zhou et al., 2018; Fig. 1b) and the fault zone width (FZW; Ajorlou et al., 2021) using OIC methods. In the case of stereo acquisitions, HR optical imagery also allows for modeling the surface topography and measuring topography change (e.g., Antoine et al., 2021, 2022; Barnhart et al., 2020, 2019; Delorme et al., 2020; Zhou et al., 2015). However, HR images are usually accessible only through purchase or with agreement with satellite agencies (exceptions of freely available samples exist but only over limited regions, i.e., in the case of disasters programs), and do not cover the entire globe surface. Moreover, HR images have a smaller spatial coverage (<20x20 km), and are generally provided as non-orthorectified products, meaning that they present distortions due to acquisition geometry (viewing angle and satellite attitude parameters). As a result, HR OIC requires accurate image orthorectification to be performed beforehand, which consist in a careful modeling of the camera attitude parameters and ground topography, and projection of the stereo optical images into a common ground geometry (Leprince et al., 2007; Rupnik et al., 2016; Shean et al., 2016).

For image orthorectification and vertical displacement measurement, accurate Digital Elevation/Surface Models (DEMs/DSMs) from pre- and post-earthquake periods are therefore needed. However, global-coverage DSMs and/or DEMs are generally available at resolutions of >30 m (e.g., ALOS30, NASA/SRTM, Copernicus , ASTER). HR DSMs and/or DEMs are generally available only locally in some limited regions of interest, usually from previous scientific publications (e.g., Antoine et al., 2022; Willis et al., 2019), or available for purchase over wider areas (e.g., ALOS World 3D). Moreover, calculating DSM from HR optical imagery requires availability and access to stereo data with acquisition parameters compliant with stereophotogrammetry requirements (e.g., complementary viewing angles, access to the acquisition parameters) (Hasegawa et al., 2000; Yin et al., 2023). In this regard, publicly available HR optical and topography data on a global scale are essential for accurate FZ deformation analysis and feature extraction over different geological and tectonic settings (Donnellan et al., 2017; Schumann and Bates, 2018).

Towards developing a global Surface Topography and Vegetation (STV) Earth Observation System (Donnellan, 2021), in this study, we provide a quantified analysis of the impact of optical and topography data resolution on the measurement of surface displacement across the FZ from the Solid Earth fault hazard perspective. The STV mission is in development stage with a primary goal of global mapping 3-D topography and topography change subject to scientifically defined resolution and measurement accuracy across broad science and application disciplines including Solid Earth, vegetation structure, cryosphere, hydrology and coastal geomorphology (e.g., DeLong et al., 2022; Donnellan et al., 2022). Through this study, we aim to address the following questions: what is the impact of optical imagery and topography data resolution on the assessment of the FZ geometry and surface displacement using OIC methods? How does measurement accuracy evolve with data resolution? To answer these questions, we perform OIC analyses using optical imagery and DEMs/DSMs datasets of various resolutions and sources to measure the near-fault ground displacement field, using the 2021 M_w7.4 Maduo, Tibet, earthquake rupture as a case study. For different datasets or combination of them, we analyze the signal to noise ratio in the obtained ground displacement maps, and its impacts on the determination of the FZ geometry, the FZW, and the associated displacements.

2. Study site and available observations

The 2021 M_w7.4 Maduo earthquake ruptured bilaterally and with a strike-slip left-lateral mechanism the Jiangcuo fault, located within the Bayan Har block of the Eastern Tibetan plateau (e.g., Fan et al., 2022; L. He et al., 2021; Liu et al., 2022; Wei et al., 2022). This earthquake generated a 160-km long surface rupture, which has been widely characterized using several geodetic (e.g., Fan et al., 2022; K. He et al., 2021; Jin and Fialko, 2021; Liu et al., 2021; Tong et al., 2022; Xiong et al., 2022; Yang et al., 2022; Zhao et al., 2021), field (Pan et al., 2022; Ren et al., 2022, 2021; Xie et al., 2022; Yuan et al., 2022) and seismic data (e.g., Li et al., 2022; Liu et al., 2021; Wei et al., 2022; Zhang et al., 2022). Field data report sparse surface ruptures with up to 2.6-2.9 m of horizontal displacement detected locally along primary fault strands (Pan et al., 2022; Ren et al., 2022, 2021; Xie et al., 2022; Yuan et al., 2022). The total horizontal surface displacement measured from OIC is 2.27-2.35 m, and occurs over a FZW of 30 m to 2.15 km (Antoine, 2024; Li et al., 2022; Fig. 1). Thanks to the extensive imagery archives and pre-existing studies, this event represents a good case to assess the effects of different optical imagery resolutions (0.5-10 m) on resolving the surface displacements across the FZ. Moreover, the rupture area is free of vegetation, snow and human activities, which makes it ideal for OIC applications. We focus on a specific region of the 2021 Maduo rupture, located at 45 km to the north-east of the epicenter, where both complex fault geometry, and distributed and diffuse deformations were documented (Antoine et al., 2024; Li et al., 2022; Li et al., 2023). Along this section, a separate analysis using HR optical data revealed an average surface displacement of ~2.81 m and FZW of ~363 m (Antoine et al., 2024; Fig. 1b).

3. <u>Data and Methods</u>

3.1. Optical and topography data

This work uses optical imagery and topography data of various resolutions provided by different space agencies to perform image orthorectification and OIC (Tab. S1). The results are combined with pre-existing OIC (Antoine et al., 2024) and SAR results (Liu et al., 2022) for further analysis. Pre-existing OIC results include pre-earthquake SPOT6/7 and post-earthquake Pleiades OIC at a common 0.5 m ground resolution, and Sentinel2 OIC at a 10 m ground resolution (Antoine et al., 2024). Pre-existing SAR results are derived from differential interferometric SAR (InSAR, DInSAR), pixel offset-tracking (POT), multiple aperture InSAR (MAI), and burst overlap interferometry (BOI) measurements at a ground resolution of 100 m (Liu et al., 2022). Optical imagery datasets used in this study include WorldView1/2/3 and Planet images, at resolutions of 0.39-0.67 and 3.125 m, respectively (Tab. S1). Planet images are downloaded as orthorectified products, whereas WorldView1/2/3 images correspond to non-orthorectified images. We also use downsampled versions of the WorldView orthoimages we produce (see 3.2. for details on orthorectification) to analyze separately the effect of image resolution from other effects, including sensor quality and image orthorectification which vary for different satellite agencies. This approach also allows us to extend the tested image resolutions (every 1 m from 0.5 to 10 m), allowing for a more complete analysis of the data resolution effect on the measurements. Topography datasets include HR pre- and post-earthquake DSMs derived from the HR tri-stereo WorldView1/2/3 images along with external and publicly available 30-m ground resolution NASA and Copernicus DEMs. Similar to the optical data, we produce downsampled versions of the HR pre- and post-earthquake WorldView DSMs to test a wide range of topography data resolutions (from 1 to 30 m) while preserving the native vertical accuracy of the stereo-DSMs (~0.5 m; Rupnik et al., 2018; Schumann and Bates, 2018; Zhou et al., 2015). The effect of DSM vertical accuracy, which primarily depend on the sensor type, is assessed by comparing the quality of OIC displacement measurements derived from orthorectifying the optical images using either the stereo-DSMs or the Copernicus and NASA DEMs.

3.2. Method

3.2.1. Optical image cross-correlation (OIC)

Optical image cross-correlation (OIC) is a technique that allows for measuring the continuous displacement of features between spatially co-registered images (Leprince et al., 2007; Puymbroeck et al., 2000; Rosu et al., 2015). Using satellite (or airborne) images acquired at different time periods, one can monitor the ground surface evolution (e.g., Bontemps et al., 2018; Dehecq et al., 2015). In this study, we use the MicMac OIC method (Rosu et al., 2015; Rupnik et al., 2017) based on a 2D statistical feature matching exploiting the color information from the pixels (0-255 in panchromatic images) to measure ground surface displacements between pre- and post-earthquake orthorectified images. In practice, one defines a correlation window size which determines the width of the group of pixels that will be used for the statistical matching. At every pixel position in the pre-earthquake image, the correlator considers the pixel color pattern within this correlation window, and searches for the best matching pattern in the post-earthquake image (correlation score from 0 to 1). The search window width in the post-image is set based on a priori knowledge of the surface displacement, generally from seismic, field or other geodetic observations, to constrain the search area to a reasonable region, and limit the calculation time and matching errors. The search window moves across the post-earthquake image with step ranging from 1 to 1/20th of a pixel through an iterative correlation process, allowing for sub-pixel displacement detection.

In this study, we performed OIC for all datasets using the same parameters, including a 5 pixels-wide correlation window, a search window of ±2.5 m, and a regularization of 0.3. These parameters can be adjusted to improve the OIC results in each case but, in a matter of consistency for the sensitivity study, we use common parameters throughout the study. The cross-correlation products consist in pixel displacement maps, in the x and y directions of the images, which correspond to the east-west and north-south direction of the orthorectified images, along with a correlation score (0-1) map (Fig. S1). The correlation score map can be used to filter the OIC results, and weight the displacement measurements (Fig. 2, steps 6 and 7). A wide range correlation parameters (e.g., Cofaru et al., 2010; Rosu et al., 2015) and filtering techniques (e.g., Andreuttiova et al., 2022; Stumpf et al., 2018) can be used to improve the OIC result for each dataset. However, the combined effects of these techniques and parametrizations are numerous, can vary for each dataset, and are thus not directly addressed within the scope of this study which primarily focuses on the effect of the data resolution. However, through simple tests on some of the datasets (Fig. S2) as well as comparison with other published measurements (Tab. 1), we briefly attempt to assess some possible effects of different processing techniques and parametrizations.

3.2.2. Complete processing pipeline

The processing pipeline used in this study to perform OIC of stereo images includes 7 major steps. Alongside the MicMac software, this work requires the use of GDAL for data cropping and resampling, Stackprof tool for stacked displacement profile extraction (see also section 3.2.3.), and python scripts for compilations of the measurements and statistics. This pipeline is similar to those applied in most photogrammetry and OIC approaches (e.g, Aati et al., 2022; François Ayoub et al., 2009; Shean et al., 2016), though they all present small differences depending on the type of data and software used. As mentioned earlier, differences in the correlation method and approach can lead to some differences in the resulting product (Avouac and Leprince, 2015; Bickel et al., 2018; Dematteis and Giordan, 2021; Montagnon et al., 2023; Rosu et al., 2015). Based on existing comparative studies (e.g., Bickel et al., 2018; Dematteis and Giordan, 2021; Montagnon et al., 2023; Rosu et al., 2015) as well as comparable measurements on similar sites (e.g., Antoine et al., 2024, 2022, 2021; Barnhart et al., 2020; Cheng and Barnhart, 2021; Li et al., 2023; Milliner et al., 2021; Tab. 1), we consider the effect of data resolution to be consistent across OIC approaches.

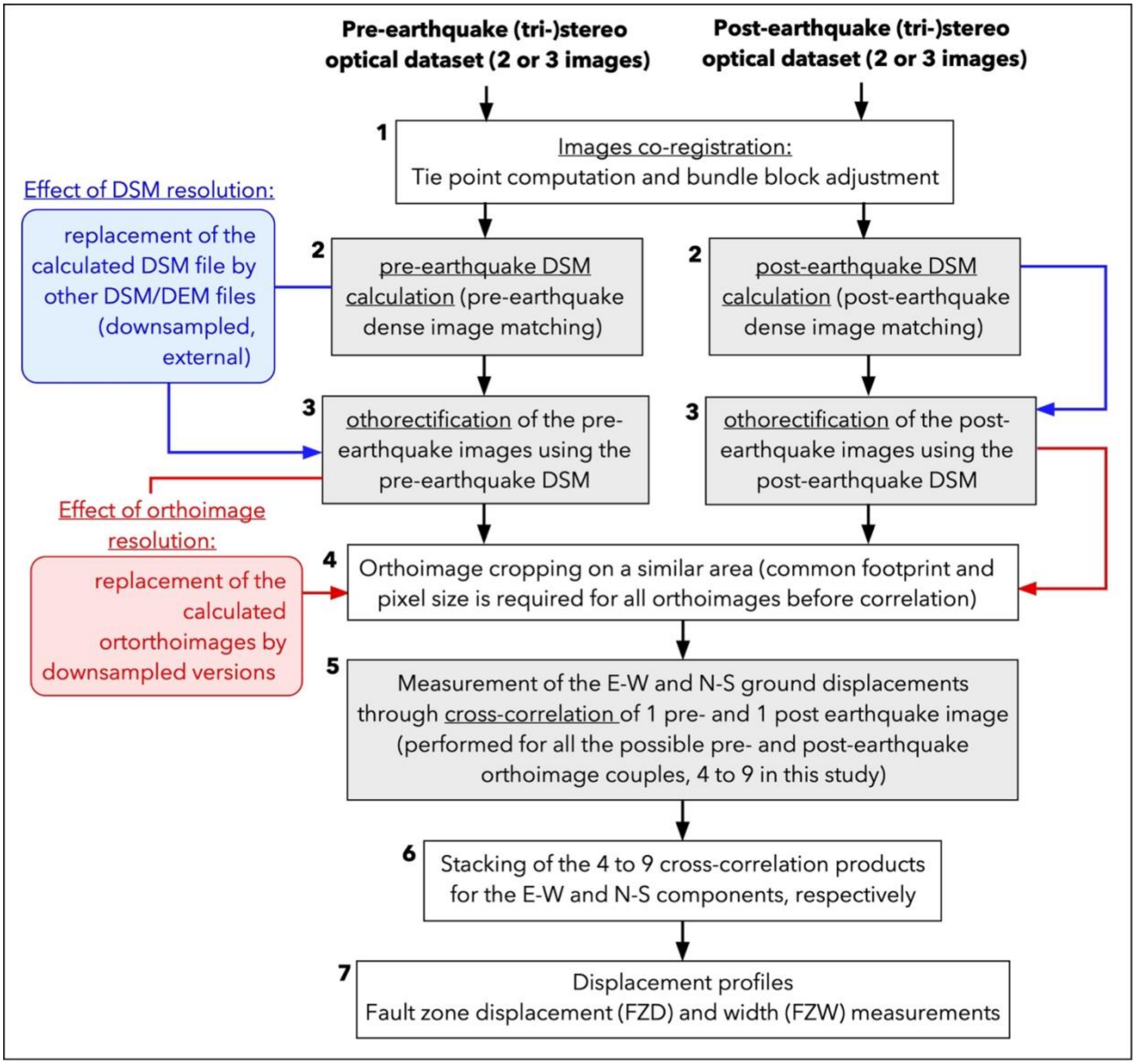

Figure 2. Diagram describing the processing pipeline applied in this study, based on the use of the MicMac photogrammetry and image cross-correlation software (Rosu et al., 2015; Rupnik et al., 2016). The pipeline includes 7 steps. Steps 2 and 3 are performed separately between the pre-earthquake and post-earthquake datasets, whereas other steps involve both pre- and post-earthquake datasets together. Grey steps correspond to the steps leading to output products including DSMs (step 2), orthoimages (step 3), and OIC maps (step 5). Tests

using external and/or resampled datasets, highlighted in color on the side of the diagram, take place at steps 3 and 4, respectively.

Step 1 consists in image co-registration through tie point detection (identification of common features across images), and bundle block adjustment (refinement of camera calibration and orientation; Rupnik et al., 2016). This step is performed commonly to the pre- and post-earthquake images to improve their co-registration accuracy. Step 2 calculates pre- and post-earthquake DSMs separately from the dense matching of the pre- and post-earthquake image pools for which orientation has been refined earlier (Step 1). Step 3 is the image orthorectification, performed individually for each image using the DSMs/DEMs of the corresponding period. Orthorectifying the pre- and post-earthquake images using separate pre- and post-earthquake DSMs prevents introducing noise from earthquake-related topography changes. Step 4 consists in cropping all orthoimages onto the same footprint, generating datasets with similar georeferencing, pixel size and pixel number for the OIC purpose. This step can be done automatically if images are precisely co-registered, or manually by locating common features in the images. Only then, image sub-pixel cross-correlation (OIC) can be performed, at Step 5. In the case of stereo (2 images) or tristereo (3 images) datasets, OIC is performed between all the possible pre- and post-earthquake orthoimage couples, which in this study represent a maximum of 9 combinations. At Step 6, the different OIC products are stacked, separately for the x (east-west) and y (north-south) components, using a weighted median method based on the OIC correlation score map (Delorme et al., 2020). Finally, at Step 7, across-fault displacement profiles are extracted to analyze the across-fault displacement offsets, and build FZ displacement (FZD) budget and FZ width (FZW) evolution (see section 3.2.3.). The complete processing pipeline is applied to the cases of the non-orthorectified HR optical images (WorldView in this study, similar pipeline applied to SPOT and Pleiades in Antoine, 2024). However, some data correspond to orthorectified products (Planet, Sentinel) that were already processed from steps 1 to 3 directly by the space agencies, using a different strategy generally based on the use of global LR DEMs. In this case, data only require processing from Step 4 to 7.

Tests on the effect of DEMs/DSMs resolution on the orthorectification and OIC products are performed by replacing, at Step 3, the original DSM calculated from the stereo images by the tested topography dataset, cropped over the same area and resampled with the same pixel size. Tests on the effect of optical image resolution, apart from those performed on the datasets originating from different sensors, are performed by using, in Step 4, downsampled versions of the high-resolution orthoimages originally obtained from the tri-stereo WorldView dataset, in Step 3. Downsampling of both the DSMs and the orthoimages is performed using GDAL.

3.2.3. Displacement profiles, and FZ displacement and FZW measurements

This study focuses on the measurement of the fault zone displacements (FZD) and width (FZW) which represent two main parameters generally considered in earthquake surface displacement analysis (e.g., Antoine et al., 2024, 2022, 2021; Gold et al., 2021, 2015; Li et al., 2022; Milliner et al., 2021; Teran, 2015; Zinke et al., 2019). To do so, we use stacked-profiles placed perpendicularly to the FZ every 200 m along the study area (StackProf tool), representing 44 profiles in total. Profile width is set to be 200 m, which was estimated as a good trade-off between noise reduction and conservation of the signal complexity (Li et al., 2022). Within the profile box, displacement measurements are stacked using a weighted median method based on the OIC correlation score map. Displacements initially obtained in the east-west and north-south components are projected, using the local azimuth of the inferred FZ, onto the fault-parallel and fault-normal directions. For the case of the 2021 Maduo earthquake, left-lateral displacement is the primary component of the surface displacement (Fig. 1), hence the measurements are focused on the fault-parallel component.

For each profile, we fit linear regressions to the displacement values outside of the inferred FZ, and assess the FZD by measuring the displacement offset between these two regressions (e.g., Antoine et al., 2024, 2022, 2021; Gold et al., 2015; Li et al., 2022). We also report the width of this offset, that corresponds to the FZW. In this study, we focus on measuring the maximum offset between the two regressions, which represents the total surface displacement across the FZ. We do not quantify the separate contributions of the localized surface slip and that of the more distributed and/or diffuse deformation, which has been the focus of another study (Antoine et al., 2024). Uncertainty on each FZD measurement, given by the StackProf tool, considers the error on the linear regressions on both sides of the FZ. Uncertainty on the FZW, however, is essentially epistemic and related to the choice of the FZ location by the operator (Reitman et al., 2022). It is generally poorly documented in the studies, and there exists no unique method to assess such uncertainty. In this study, we choose to assess the FZW uncertainty by measuring a minimum and maximum FZW for each profile along with a preferred FZW for which the FZD was assessed, method previously used by Gold et al. (2015).

4. Results

4.1. Impact of optical image resolution on the OIC results

4.1.1. Images acquired by different satellite sensors

In this section, we compare ground displacement measurements obtained from the OIC of images acquired by different satellite sensors and with resolutions ranging from ~0.5 to 10 m (Figs. 3, 4, S1 and S3, and Tabs. S1 and S2). We also compare these results with the displacement maps derived from SAR measurements (Liu et al., 2022) at a 100 m resolution.

4.1.1.1. Surface displacement and curl maps

We present the east-west (E-W) component of the displacement field (north-south (N-S) component presented in Figure S1) along with curl maps, which were derived from the E-W and N-S displacements (Figs. 3g,h, and S3). Visual analysis of the displacement maps obtained from the OIC of the different imagery datasets first highlights a consistent E-W displacement offset of amplitude ±2 m. Transition between the NE and SW regions of the study area, which were displaced in opposite directions, occurs along an oblique structure lying at the center of the study area, corresponding to the FZ. Even though, at a first order, consistency is observed between the different results, we also highlight the differences in the signal to noise ratio, impacting the inferred FZ geometry and associated FZD and FZW measurements. Spatially coherent noise first arises from topography residuals due to camera attitude parameter estimations and DEM errors (Fig. 2, steps 1-3). Such noise is common for data downloaded as orthorectified products, and for which orthorectification is not always performed using a refined camera model nor a HR and accurate DEM/DSM (Fig. 2, step 1). Noise also occurs in regions of lesser surface texture change, where the correlator cannot identify common pixels between the pre- and the post-earthquake images, with common sources that are vegetation, snow, water, and clouds. Finally, high-frequency noise arises from random cross-correlation error, especially enhanced by image noise (Bornert et al., 2018, 2009; Su and Zhang, 2016).

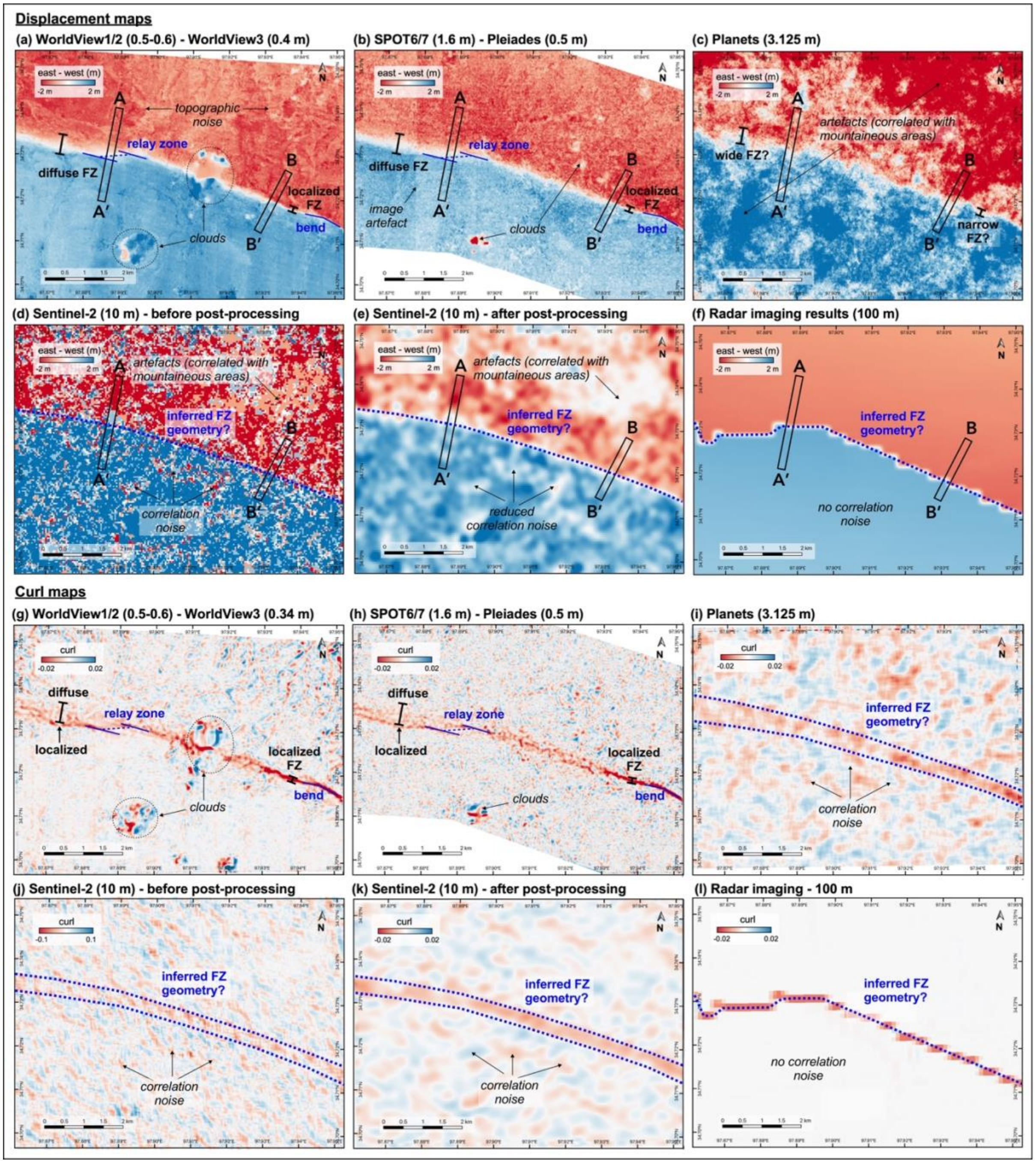

Figure 3. (a-f) East-west (E-W) surface displacements along the study site calculated from the OIC of images originating of different sensors and of different resolutions (Tab. S1), and

comparison with SAR-derived measurements from Liu et al. (2022). AA' and BB' across-fault displacement profiles are presented in Figure 4. (g-l) Map of the curl (ω) calculated from the E-W (u_x) and N-S (u_y) downsampled and filtered (Fig. S3) displacement maps using the following relation $\omega = \nabla \times \mathrm{U} = \frac{\partial u_y}{x} - \frac{\partial u_x}{y}$ (Zhou et al., 2018). Negative curl (red) corresponds to anti-clockwise rotation and is consistent with the left-lateral mechanism of the 2021 Maduo rupture.

Among the different results, those obtained from HR imagery (Fig. 3a,b) allow for describing spatial variations in the FZ geometry, and separating the diffuse deformation regions, especially to the NW of the study area, from the localized ones. Fault bends and relay zones can also be observed along the FZ in these maps (blue lines in Fig. 3a,b). Such complex FZ geometry is particularly highlighted in the curl maps including, for example, asymmetric and mixed diffuse and localized patterns across the FZ to the NW of the study area. Across both HR displacement and curl maps, such complex patterns are consistently observed (Figs. 3a,b,g,h, S1a,b, and S3a,b). Small differences include greater topography-correlated noise in the WorldView OIC result (as well as decorrelation due to the presence of a cloud across the FZ), and greater background noise in the SPOT/Pleiades OIC result. Greater background noise in the SPOT/Pleiades OIC likely arises from the fact that SPOT6/7 images were upsampled to the 0.5 m native resolution of the Pleiades images (Antoine et al., 2024), possibly leading greater random correlation, especially among upsampled pixels.

Results obtained using LR imagery (Fig. 3c,d,e) present a smaller signal to noise ratio, resulting in a spatially heterogeneous displacement field both across and outside of the FZ. Noise is particularly visible in the regions outside of the fault zone (>1 km), where one would rather expect about constant displacements as shown in the HR results. In the curl maps, noise arises as high-frequency displacement variations, especially visible in the regions outside of the FZ, and with amplitudes similar to that of the curl signal across the FZ (Fig. 3i,j,k). Noise standard deviation (std, analyzed to the NE of the inferred FZ within the mountainous areas, Fig. S4) increases with decreasing image resolution, from a std of 0.30 m in the WorldView OIC results to a std of 1.76 m in the Sentinel-2 OIC results (raw result, no filtering). After filtering and smoothing of the Sentinel-2 results, background noise reduces with now a std to 0.47 m (Fig. 1e,k; see Antoine et al., 2021 for methodology). Nevertheless, filtering and smoothing fails to help retrieving the high-resolution information on the FZ geometry as well as removing the low-frequency noise. As a result, the FZ primarily shows up as a continuous and curved structure absent of geometrical complexity in the LR displacement results. The FZ identification and FZD and FZW measurements in the LR results are then subjected to ad hoc interpretations, and are not always consistent from one displacement product to another.

As a case example of comparison between OIC and SAR measurements in the near-fault domain, we compare our results with the SAR-derived displacement maps from Liu et al. (2022) (Fig. 3f,l). The SAR results present a 100 m ground resolution and a cm-scale accuracy, which is consistent with the characteristics of typical multi-look SAR-derived products used to image earthquake ground displacements (e.g., Fielding et al., 2013; He et al., 2023; Jin and Fialko, 2021; Massonnet et al., 1993; Socquet et al., 2019; Tong et al., 2022; Zhao et al., 2021). Displacement amplitudes between the SAR and OIC measurements are consistent at the first order. However, at the scale of the study area, the FZ location and geometry reported by the SAR measurements is incorrect with regard to both the LR and HR OIC results. This observation supports the previous inference that, in the near-fault domain, measurements derived from SAR data are generally less accurate than those derived from optical data.

4.1.1.2. Displacement profiles, and fault zone displacement budget, and fault zone width evolution

Displacement profiles (see section 3.2.3 for methodology) are used to assess the evolution of the FZD and FZW along the study area, for the different displacement products (Figs. 3 and S1). We first present the analysis of two separate displacement profiles, and then assess the along-strike FZD budget and associated FZW evolution. The two profiles include one profile across a wide FZ, characterized primarily by diffuse deformation (AA' in Figs. 3 and 4a), and one profile across a narrower FZ, characterized primarily by localized deformation (BB' in Figs. 3 and 4a). We first observe that the two displacement profiles, when taken across the HR results (red and blue profiles in Figure 4a), report similar displacement patterns. These patterns include a displacement offset in the middle of the profile, of similar amplitude in both profiles, surrounded by regions of constant displacement. The position of the displacement offset corresponds to the location of the FZ. The two same profiles taken across the SAR-derived results (black profile, Figure 4a) display consistent patterns; however, in this case, the displacement offset is under-estimated, and mis-located in the case of profile BB', highlighting the lower constraints provided by SAR data in the near-fault domain.

Profiles taken across the LR displacement maps (green, orange and pink profiles, Figure 4a) show displacement variations both at low- and high-frequencies, making the determination of the displacement offset and the associated FZD and FZW more challenging. In fact, these profiles do not allow for a clear identification of the FZ location. Uncertainties on the measured FZD and FZW are then on the order of a few tens of centimeters and hundreds of meters in amplitude, respectively. Uncertainty in the FZW measurement is even larger than the measured value itself, revealing the arbitrary nature of the FZ location and geometry determination when using the LR results compared to the HR results. Uncertainty on the FZD and FZW measurements, for the profiles AA' and BB' respectively, increases by a factor of ~10-100 and of ~2 from the HR to the LR results (Fig. 4a).

Analyzing the stacked profiles every 200 m along the study area, 44 profiles in total, we assess the FZD (Fig. 4b, and Tab. S2) and FZW evolutions (Fig. 4c, and Tab. S2) along the FZ strike. Measurements derived from the HR results show great consistency (blue and red curves in Fig. 4b,c) with an average difference in the FZD measurements of ~2% between the WorldView and the SPOT/Pleiades results. Maximum differences along individual profiles reach ~0.5 m, which is less than 20% of the average FZD (2.74 ± 0.007 m and 2.81 ± 0.009 m for the WorldView and SPOT/Pleiades OIC results, respectively). Local differences, in this case, can be explained by variations in the noise from one dataset to another (e.g., presence of a cloud across the FZ in the WorldView3; Fig. 3a) which then disrupts the FZD and FZW measurements.

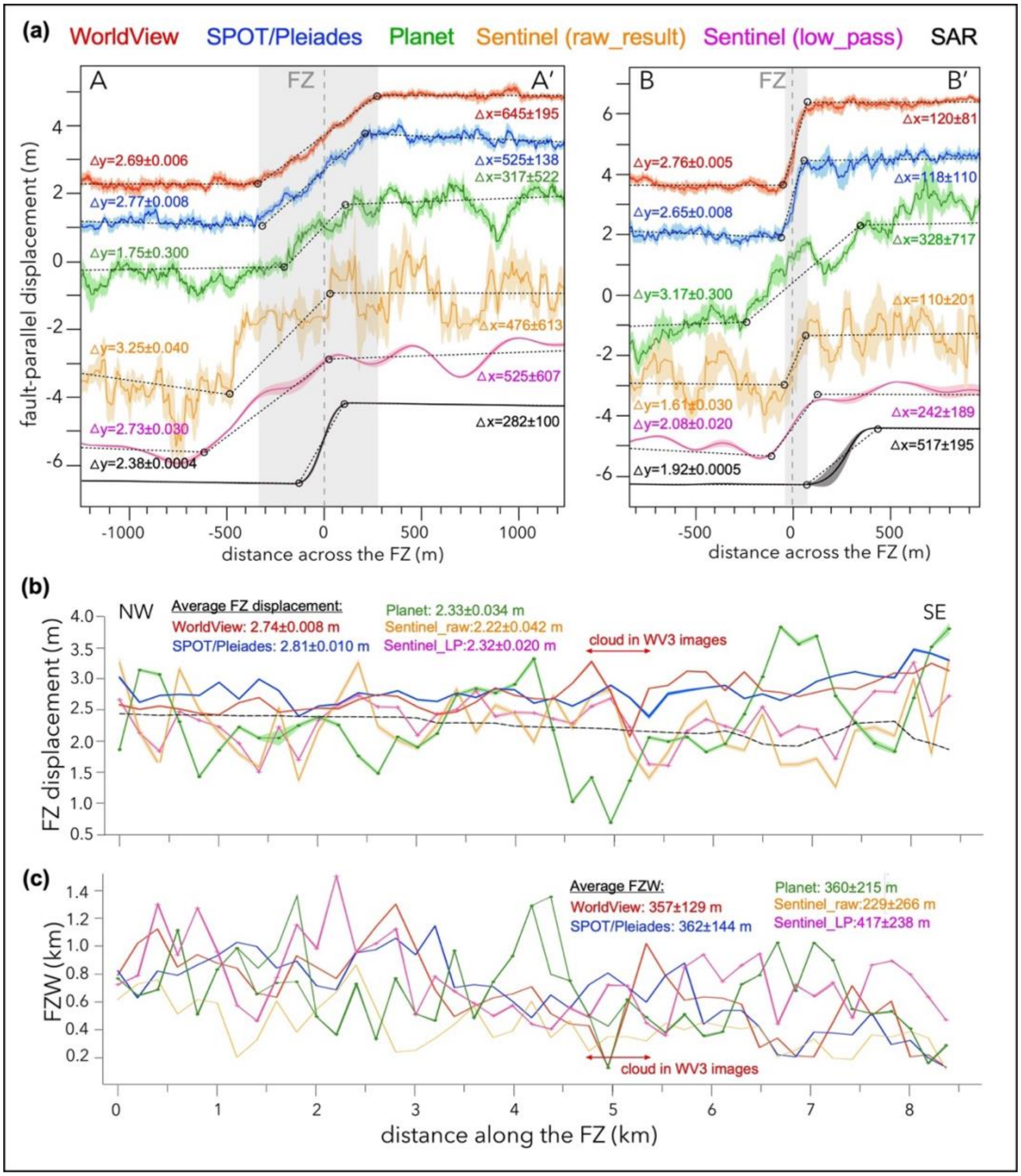

Figure 4. (a) Across-fault stacked displacement profiles, in the fault-parallel component, placed across the FZ in the displacement maps derived from the OIC of different satellite sensors optical data (Fig. 3a-f). Dashed black lines are the linear regressions, and black circles are the piercing points used for the displacement offset measurements. FZD (Δy, in m) and FZW (Δx, in m) are indicated on the left and right side of the profile, respectively. (b) FZD budget (m) in the fault-parallel component, derived from the analysis of the 44

profiles, placed every 200 m perpendicularly to the FZ (Tab. S2). (c) FZW (km) measured for each displacement offset (Tab. S2).

FZD and FZW curves obtained from the analysis of the LR displacement maps (green, orange, and pink curves in Fig. 4b,c) show significant differences, sometimes reaching ~2 m for the FZD, and ~1 km FZW. These differences reflect the increasing uncertainty in assessing the FZ location with decreasing image resolution, as a result of greater background noise. Uncertainties on the FZD and FZW measurements increase from 0.8 cm to 42 cm, and from 129 m to 266 m when using the WorldView and the Sentinel data (raw result), respectively (Fig. 4b,c). In addition, resulting from the simplified inferred FZ geometry and the un-detected diffuse deformation regions, FZD measurements derived from the LR OIC results are, on average, under-estimated by >15% compared to that derived from the HR OIC results. Filtering and smoothing of the Sentinel-2 results allow decreasing the high-frequency noise and improving the recovery of the displacement by +5% (Fig. 4b,c). However, across the different LR results, including the Sentinel-2 results before and after filtering and the Planet results, FZW measurements vary considerably around the HR reference value, obtained from the WorldView results. Therefore, FZW estimated based on LR imagery are likely unreliable compared to that obtained from HR imagery (Ajorlou et al., 2021). Still, among the LR results, that obtained from the Planet data at 3.125 m resolution seems to retrieve better the FZW evolution from narrow to the east to wider to the west of the study area, suggesting a better sensitivity to FZ complexity compared to the Sentinel-2 data at 10 m resolution. Finally, average FZW values inferred from the Sentinel-2 measurements before and after filtering evolve from -25 to +15% around the HR reference, highlighting the influence that post-processing techniques can have on the FZW assessment in LR results (Fig. 3j,k). Among the datasets tested in this study, HR optical imagery then represents the most reliable source of information for determining the FZ location, geometry, and associated FZD and FZW.

4.1.2. Downsampled pre- and post-earthquake WorldView orthoimages

To separate the effect of data resolution from other data related confounding factors (e.g., sensor type, acquisition date and geometry, orthorectification quality etc.), we performed OIC on downsampled versions of the WorldView orthorectified images, at resolutions of 1 to 10 m (Figs. 5, and Tab. S3). This analysis enables cross-examination against our previous observations made using data from different satellite sensors (Figs. 3 and 4, and Tab. S2).

Visual inspection of the obtained displacement maps shows an increase in the background noise with decreasing data resolution (Figs. 5 and 6a), arising both as topography-related noise in the mountainous area (Fig. 5a-f) and as random high-frequency noise, similar to what was found previously (Fig. 3). As a result, the identification of the FZ location and geometry is again challenging in the LR results, especially at resolutions lower than 3 m (Fig. 5). At comparable resolutions of 3 and 3.125 m, though, OIC results derived from the downsampled WorldView orthoimages (Fig. 5d) show less noise than those derived from the Planet orthoimages (Fig. 3c). Such difference most likely relates to the fact that the higher-level Planet data products are orthorectified using a low-resolution DEM, and without bundle block adjustment (Fig. 2, step 1). This observations supports the previous inference that sensor and orthorectification quality are critical parameters for reliable OIC measurements (Antoine et al., 2021, 2022; Leprince et al., 2007; Shean et al., 2016). Conversely, at a comparable resolution of 10 m, Sentinel-2 OIC results (Fig. 3d) are less noisy than those obtained using the downsampled WorldView orthoimages (Fig.

5f). This difference can arise from i) good Sentinel-2 orthoimage quality, at least compared to the Planet data, and ii) possible aliasing in the downsampled products, especially due to large downsampling factors applied (García Aranda et al., 2021).

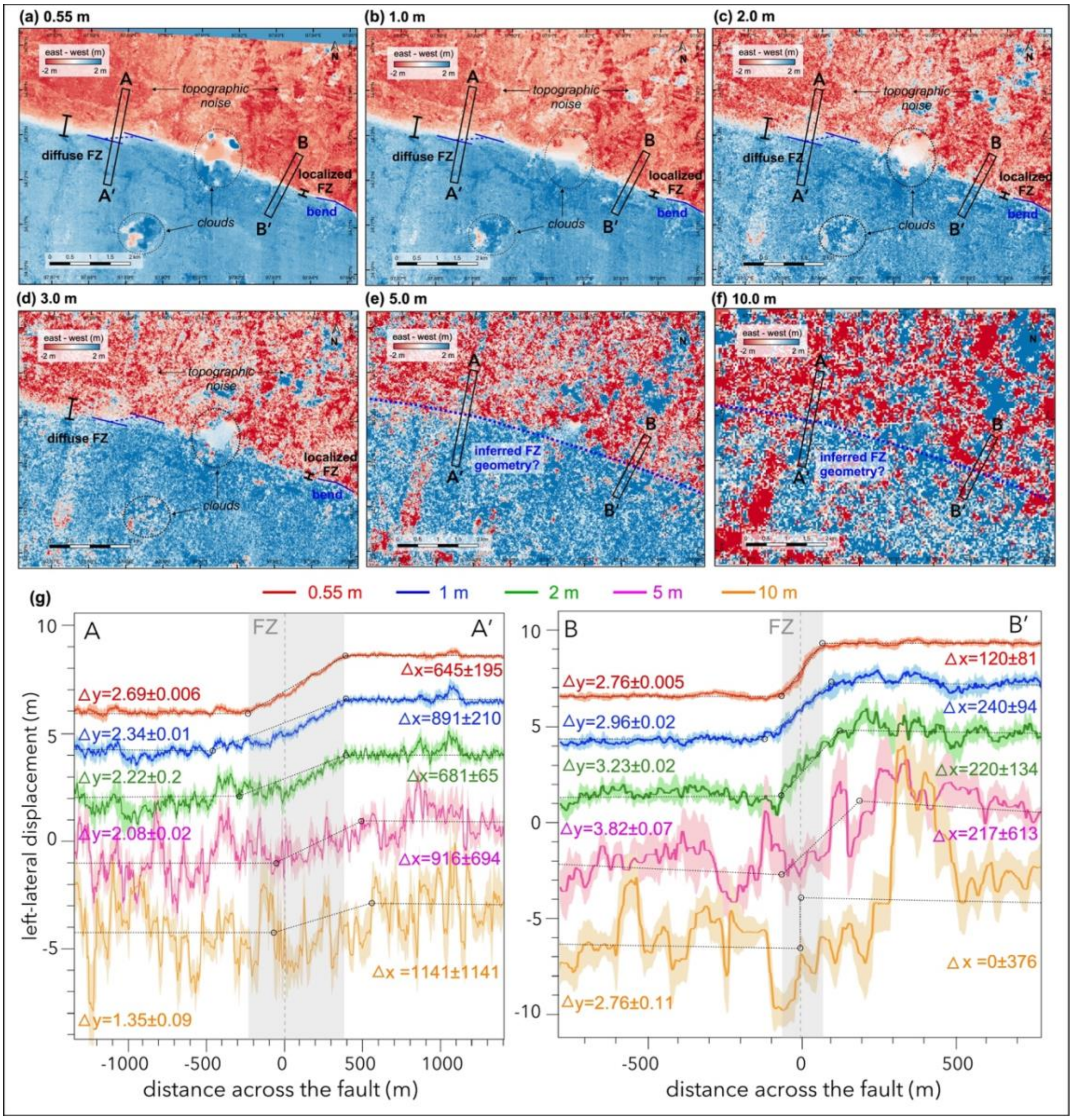

Figure 5. (a-f) East-west displacement maps calculated from the OIC of (a) WorldView and (b-f) downsampled WorldView orthoimages. No filtering is applied to the displacement map outputs, and similar correlation parameters are used for all correlations. FZ and noise

features are highlighted (similar to Fig. 3). (g) AA' and BB' across-fault stacked displacement profiles in the fault-parallel component. Similar to Figure 4, FZD and FZW values, and associated regression profiles are indicated. Units are meters.

Profiles taken across the displacement maps show an increase in background noise with decreasing orthoimage resolution (Fig. 6a), which is particularly reflected by the std of the FZD and FZW measurements. We estimate an increase in the measurement's std with decreasing orthoimage resolution by a factor 15 and 20 for the FZD, respectively for AA' and BB', and ~5 for the FZW (similar in AA' and BB'). Considering all the measurements together, we find a linear increase of the standard deviations (stds) for both the FZD and FZW measurements with decreasing orthoimage resolution (Fig. 6b,c). For resolutions greater than 5 m, the signal to noise ratio approaches 1 (Fig. 6a), and the estimation of the FZW and associated epistemic uncertainty is subjected to the choice from the operator. On average, FZW and FZD estimations are underestimated by a factor 0.78 and 0.70, respectively, in the 10-m results as compared to the 0.55 m results (Fig. S5 and Tab. S3).

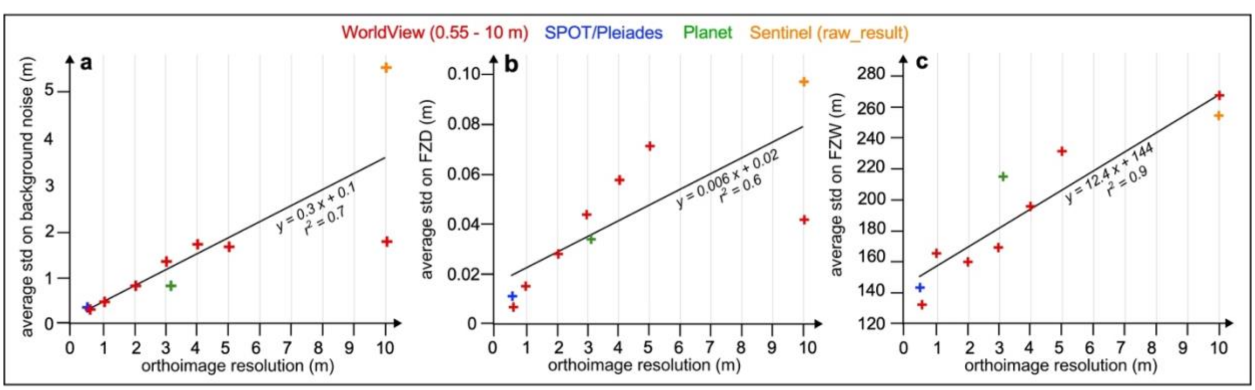

Figure 6. Evolution of the average standard deviation (std) associated with (a) the background noise NE of the FZ (Fig. S4), and the (b) FZD and (c) FZW measurements with

decreasing orthoimage resolution. Points with different colors correspond to the results from the multi-sensor study (Figs. 3 and 4). Red points correspond to the results based on the WorldView orthoimages, both at native and degraded resolutions (Fig. 5). Black lines are linear regressions calculated for all datapoints, with r^2 the associated correlation factor.

4.2. Impact of DSM/DEM resolution on the OIC result

We test the effect of using DEMs/DSMs of different resolutions, acquisition sensors, and dates on optical image orthorectification and derived OIC quality (Fig. 7). To do so, we performed OIC on the WorldView1/2/3 image pool orthorectified using different DEMs/DSMs datasets including i) the high-resolution WorldView DSMs derived from those same images (Fig. 7a), ii) downsampled versions of these HR DSMs (1-30 m; Figs. 7a-c, and S6b-d) as well as iii) publicly accessible 30-m-resolution DEMs from the NASA and Copernicus space agencies (Figs. 7d,e, and S6e,f). Downsampling of the DSMs preserves the native ~0.5 m accuracy of the stereo DSMs across the range of downsampled resolutions, though it reduces the high-frequency noise (Fig. S6). Thus, we can test separately the effects of topography data ground resolution (0.55-30 m), vertical accuracy (~0.5m in the WorldView DSMs, and several meters in the NASA and Copernicus DEMs; see Fig. S5 and S6), and acquisition time (pre- and/or post-earthquake) on the OIC quality, and FZD and FZW measurements.

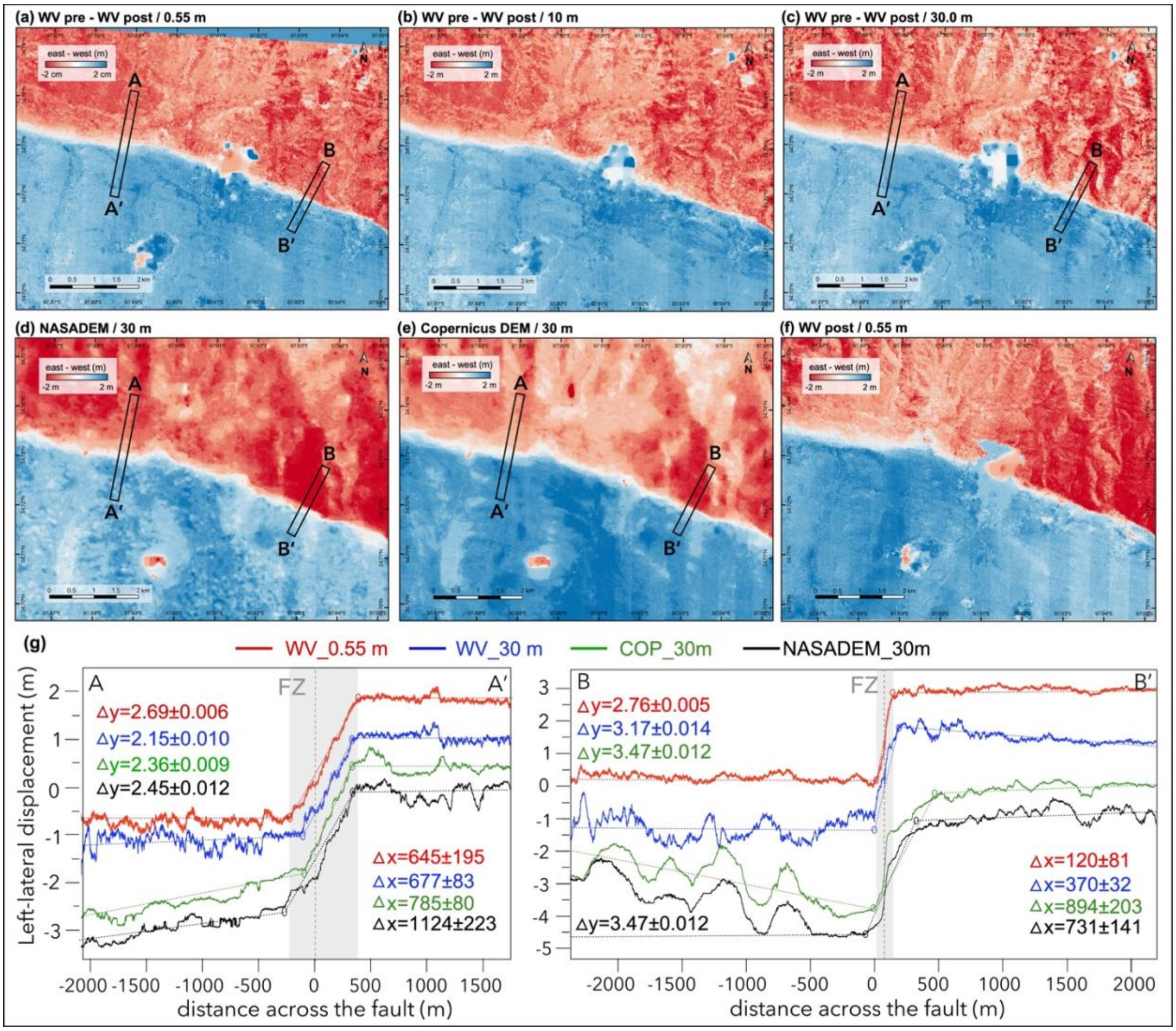

Figure 7. East-west displacement maps calculated from the OIC of 0.55-m resolution WorldView images orthorectified using (a) high-resolution pre- and post-earthquake WorldView DSMs, (b-c) downsampled version of the pre- and post-earthquake WorldView DSMs, (d-e) the NASA and Copernicus global DEMs (from the pre-earthquake period), and (f) the high-resolution post-earthquake WorldView DSM. No filtering is applied to the displacement maps, and similar correlation parameters are used for all OIC (see Fig. S2 for tests on other parameters). (g) AA' and BB' across-fault stacked profiles in the fault parallel

component across (a) in red, (c) in blue, (d) in black, and (e) in green. Profile annotations are similar to Figure 4.

Visual analysis of the displacement maps obtained from the different orthorectified WorldView products show consistent ground displacement patterns, including the FZ location and geometry (Fig. 7a-f). This suggests that the effect of the DEM/DSM resolutions (Fig. 2) is less significant than that of the optical image ground resolution itself though the processing chain. Particularly, similar patterns are observed across the results based on the downsampled, 1 to 30 m resolution, stereo DSMs for images orthorectification. These results confirm that the DEM/DSM ground resolution, as an individual parameter, has minor impact on the orthorectification and OIC quality (Fig. 7a-c; displacement budget and FZW evolution in Fig. S8). Although larger topography-related noise appears when using DSMs of resolution >10 m (Fig. 7c), resulting in greater variability in the FZD and FZW measurement (Fig. 7g). This variation shows no clear correlation with the DSM ground resolution across the range 10-30 m, and remains on average, within a confined range of -3 and 0%, and -12 and 0.5% around the HR measurement references for the FZD and FZW, respectively (Fig. 8, and Tab. S4).

Displacement maps obtained from the OIC of the WorldView images orthorectified with the Copernicus (Fig. 7e) and NASA DEMs (Fig. 7f) are in general smoother and with larger topographic noise than what previously described when using the downsamped WorldView stereo DSMs. This is particularly visible in the displacement profiles, where low-frequency noise affects the displacement trends outside of the FZ, resulting in more variable and, on average, over-estimated of FZD and FZW measurements (Figs. 8 and S9, and Tab. S5). The topography-related noise being consistent with the estimated vertical uncertainty (several meters) of the global DEMs (Brosens et al., 2022; Florinsky et al., 2018; Uuemaa et al., 2020; Zhou et al., 2018), we suggest that the DSM vertical accuracy has a direct effect on the OIC result. Noise can also arise from topography translations on one side of the post-earthquake image compared to the pre-earthquake image due to the earthquake ground displacement, an effect that was not taken into account when using the global DEMs acquired before the earthquake event (Fig. 7f). We assess the effect of such topography translation by performing the orthorectification of the WorldView images using only the post-earthquake WorldView DSM (Fig. 7f). Results indeed show topography-related noise and low frequency artefacts in the similar areas as in the results based on the NASA and Copernicus DEMs, suggesting that part of the noise observed in those three results might arise from the topography translation due to the earthquake ground displacement. Finally, geographic mis-alignment between the images and topography datasets, especially when using external source DEMs that were not processed jointly with the images when refining the camera model (Shean et al., 2020) can also lead to similar type of noise. Through comparison of the differences between the pre-earthquake WorldView stereo DSM (derived from the images) and the external DEMs in the same reference frame (Fig. S7), we assess this effect to be negligeable, at least in the case of the NASADEM (Fig. 7a), although it cannot be fully excluded.

5. Discussion, and implications towards the development of the Surface Topography and Vegetation (STV) Earth Observation System

In this study we investigated the impacts of important characteristics of the optical imagery and topography data, especially the ground resolution, on accurate imaging of earthquake ground displacement field. Figure 8 summarizes the average FZD and FZW measurements from the different tests performed in this study. Based on our main observations along with published results for other earthquake ruptures (Tab. 1), we highlight important characteristics of optical imageries and DEMs/DSMs that should be considered for FZD and FZW measurements using OIC methods, and implications for the development of future Earth Surface Topography Observation Systems, especially from the fault-related hazard perspective.

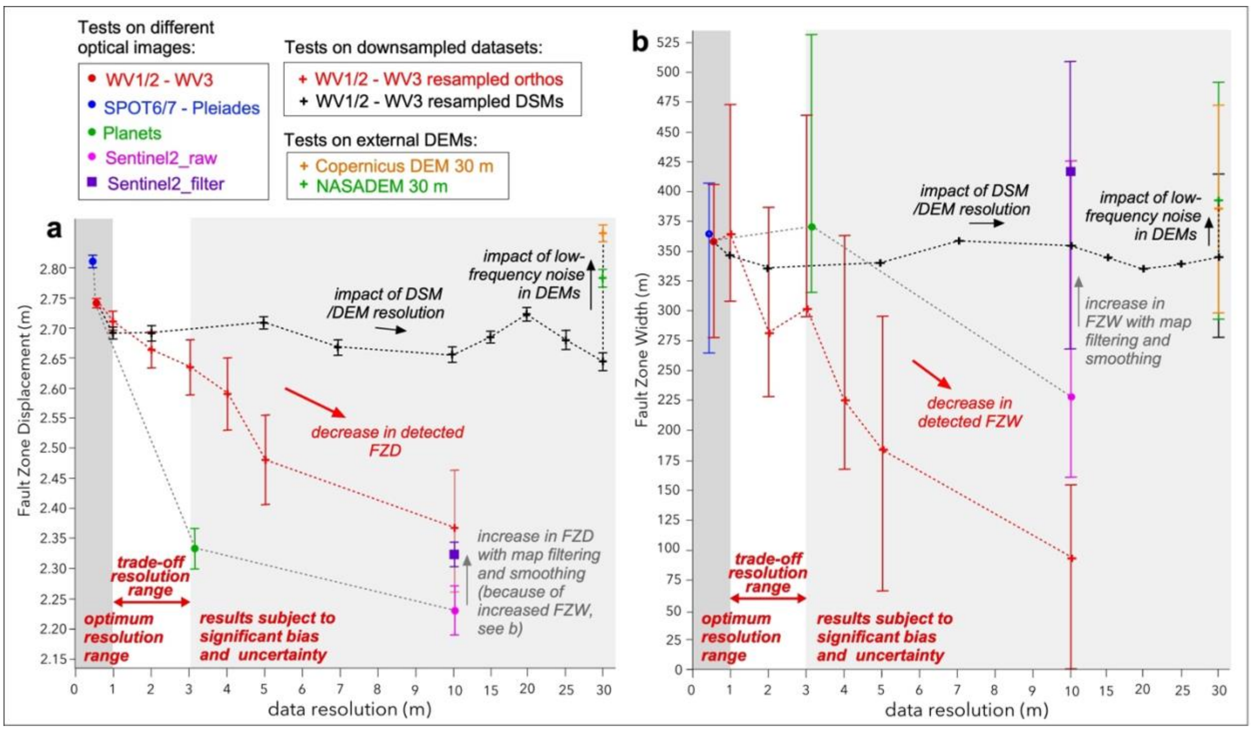

Figure 8. Synthesis of the average measurements of (a) Fault Zone Displacement (FZD) and (b) Fault Zone Width (FZW) obtained from the different OIC tests performed in this study (Figs. 3, 5, and 7). Data points include tests using optical imagery originating from different sensors (colored circles and square, trend in dashed grey), the downsampled WorldView orthoimages (red crosses, trend in dashed red), the downsampled WorldView DSMs (black crosses, trend in dash black), and the Copernicus and NASA DEMs (orange and green crosses, included in the dashed black line). Difference between the WorldView and

SPOT/Pleiades FZD measurements at similar resolution can be explained by the presence of a cloud across the FZ in the WorldView3 images (Fig. 4b).

5.1. Effect of optical image ground resolution on the measurement of horizontal surface displacements using OIC techniques

Using optical images acquired by different satellite sensors along with downsampled versions of the WorldView dataset, we showed a consistent decrease in the FZD and FZW average measurements with decreasing image resolution (red and grey curves; Fig. 8). We found that FZD are underestimated by a factor ~0.8 when using ≥10-m resolution images (e.g., Sentinel-2) compared to ~0.5-m resolution images. Under-estimation factor is calculated here as the ratio between the FZD measured in the LR Sentinel-2 and in the HR (~0.5 m) WorldView results, the latter considered to be closer to ground truth (Figs. 1b and 3a). Intriguingly, we observe a similar under-estimation of the FZD, by a factor of ~0.7-0.8, for other earthquake studies that were documented using both HR and LR optical imagery (Tab. 1). For example, in the case of the 2019 Ridgecrest, California, earthquake sequence, average surface displacement associated with the M_w6.4 and M_w7.1 events, respectively, were estimated to be 0.73 ± 0.09 m and 2.13 ± 0.06 m from WorldView images (Antoine et al., 2021), compared to 0.55 ± 0.08 m and 1.60 ± 0.22 m from Sentinel-2 images (Chen et al., 2020). Similarly, in the case of the 2013 Baluchistan, Pakistan, earthquake, average FZD derived from WorldView data is 8.3 m (Gold et al., 2015) compared to only 6 m using Landsat-8 images at 15 m resolution (Avouac et al., 2014). The fact that similar under-estimation factor on FZD measurements from LR compared to HR optical imagery is observed for different earthquakes, where different images, orthorectification strategies and OIC algorithms were used (e.g., Fig. S2), is suggesting that the optical imagery ground resolution is the primary controlling factor on the resultant OIC quality, and the derived FZD and FZW measurements accuracy. In the case of Maduo, however, average FZD estimated for the entire rupture length (~160 km) were similarly estimated from both the LR and HR data. The 2021 Maduo surface deformation was shown to be primarily diffuse and to occur over an average ~600 m FZW (Antoine et al., 2024; C. Li et al., 2022). Therefore, the optical imagery resolution effect on the FZD and FZW measurement accuracy is especially significant in the case of localized and narrow surface deformation features.

Table 1. Comparison of FZD measurements for the 2021 Maduo rupture with other continental earthquakes.

Earthquake	Sensor	Resolution (m)	Average FZD (m)	Reference
2021 Maduo (M_w7.4)	Sentinel2B	10	2.27	Li et al., 2022
	SPOT6/7/ Pleiades	0.5	2.35 ± 0.09	Antoine et al., 2024
2013 Baluchistan (M_w7.8)	Landsat8	15	6	Avouac et al., 2014
	Landsat8	15	6.7 +0.3/-0.4	Zinke et al., 2014
	SPOT5	2.5	8	Vallage et al., 2015
	WorldView	0.5	8.3	Gold et al., 2015
2019 Ridgecrest foreshock (M_w6.4)	Sentinel2B	10	0.55 ± 0.08	Chen et al., 2020
	Planet	3.125	0.56 ± 0.10	Milliner and Donnellan, 2020
	WorldView/ Pleiades	0.5	0.73 ± 0.09	Antoine et al., 2022
2019 Ridgecrest mainshock (M_w7.1)	Sentinel2B	10	1.60 ± 0.22	Chen et al., 2020
	Planet	3.125	1.68 ± 0.19	Milliner and Donnellan, 2020
	WorldView/ Pleiades	0.5	2.13 ± 0.06	Antoine et al., 2022

From these results, we suggest that the optimal image resolution for accurately measuring the FZD and FZW as well as deciphering the localized versus diffuse nature of surface deformation lies between <0.5 and ~1 m, for earthquakes of M_w>6.4 (Fig. 8 and Tab. 1). In this study, starting from a resolution of 2 m, background noise approaches ±1 m (Fig 6a), making the FZ identification more challenging (Figs. 3 and 5) and the FZD and FZW measurements less accurate (Figs. 4, 5g, 6b,c, and 7g). For resolution greater than 3 m, FZ geometry cannot be clearly identified anymore. Provided an accurate image orthorectification, image resolutions of 1-3 meters can represent an acceptable trade-off range for estimating the FZD and FZW, but not the detailed FZ structure (Fig. 3c versus Fig. 5c). Moreover, this trade-off resolution range would be mostly beneficial only to medium to large magnitude earthquakes (M_w>~6.4) that generate at least 0.5-1 m of ground displacement (Fig 6a). Detecting surface displacements of amplitudes <0.5 m, for example associated with distributed and diffuse processes and/or smaller magnitude events, requires sub-meter resolution imagery. At present, there is a lack of publicly available HR optical imagery on a global scale, presenting an opportunity that can be addressed by future Earth Surface Observation Missions such as NASA Surface Topography and Vegetation (STV) (Donnellan et al., 2021).

5.2. Effect of DEM/DSM ground resolution and vertical accuracy on the measurement of earthquake surface displacement

5.2.1. *Effect on the measurement of horizontal surface displacements using OIC techniques*

In this study, we showed that the effect of the DEM/DSM ground resolution alone was not significant on the quality of OIC results (Fig.5a-c,g and black curve in Fig. 8) in comparison with that of the DEM/DSM vertical accuracy, the latter which can relate to or be independent of the ground resolution depending on the sensor type (Radar, optical, LiDAR). In general LR global baseline DEMs derived from Radar observations have vertical errors of several meters or tens of meters, especially in mountainous areas (Brosens et al., 2022; Florinsky et al., 2018; Uuemaa et al., 2020; Zhou et al., 2018). In comparison HR stereo-derived DSMs tend to have an error about 1 meter or below (e.g., Hu et al., 2016; Rupnik et al., 2018; Wang et al., 2019; Zhou et al., 2015), and usually permit the best possible image orthorectification and OIC result (Figs. 1a and 7a-c). Therefore, even though global DEMs provide sufficient ground geometry reference for most applications, the DSMs derived from HR stereo imageries, ideally available for both the pre- and post-earthquake periods, represent a preferred topography dataset for OIC-based FZD mapping. Such highly accurate DEM/DSM products can also be obtained using LiDAR data (e.g., Donnellan et al., 2017; Scott et al., 2020). However, acquiring dense (several points per meter) LiDAR observations on a global scale is a technical challenge especially regarding the energy supply to measurement ratio. For these reasons, we suggest HR stereo optical imagery to be a good candidate for global topography measurements for future NASA Surface Topography and Vegetation (STV) Earth Observation System (Donnellan et al., 2021).

5.2.2. *Implications on vertical displacement measurements using topography differencing methods*

Near-fault vertical displacement measurements, similar to the horizontal measurements previously documented, represent a crucial information to constraining the rupture processes, both at depth and at the surface (Antoine et al., 2023; Lauer et al., 2020). Such information is especially crucial for determining possible fault dip angle variations (Teran et al., 2015; Vallage et al., 2015), stress rotations (Milliner et al., 2022) and slip deficit (Antoine et al., 2023; Fialko et al., 2005) in the shallow crust. Again, sub-meter resolution stereo optical imagery demonstrated its potential for measuring sub-meter vertical displacements of from the comparison of the pre- and post-earthquake stereo derived DSMs (e.g., Antoine et al., 2022, 2021; Delorme et al., 2020; Teran et al., 2015; Zhou et al., 2015). Applied on a global scale, submeter resolution stereo imagery then would allow for documenting complex and/or small amplitude vertical displacements over a wide range of geological and tectonic contexts and earthquake magnitudes, allowing to refine earthquake source models and our understanding of the shallow rupture processes (Antoine et al., 2023; Marchandon et al., 2021; Xu et al., 2016).

Vertical accuracy of stereo imagery DSMs and derived vertical displacement maps is proportional to the image resolution (Rupnik et al., 2018; Schumann and Bates, 2018; Fig. S10). Submeter resolution optical imagery is thus a prerequisite for accurate measurement of vertical ground displacements based on topography differencing methods. The acquisition geometry of the stereo imagery, such as the relative viewing angles between different images, is another limiting factor of the quality of the stereo DSMs and derived topography change products (Fig. S10), especially when using archive images that are not acquired with optimal viewing angles. Future stereo imagery systems then need to address these acquisition geometry requirements, which can vary depending on the topography amplitude and roughness of the area to be imaged (Hasegawa et al., 2000; Hu et al., 2016; Loghin et al., 2020). Other confounding factors such as the presence of vegetation could also limit the quality of ground change measurements. However, ongoing research starts to show the potential of overcoming these limitations and recovering the ground surface geometry in sparse vegetated regions (e.g., Yin et al., 2023). The vegetation issue can also be mitigated by combining optical imagery with dense HR LiDAR data. As mentioned before, Lidar is able to map 3-D ground surface with high resolution and high vertical accuracy. However, such data are generally acquired locally from airborne campaigns because of the greater technical challenge and cost constraints associated with global dense LiDAR acquisitions.

Conclusions

This study provides a quantitative assessment of the effects of optical imagery and topography data characteristics, primarily ground resolution, on the measurement of near-fault earthquake surface displacements using the 2021 M_w7.4 Maduo, Tibet, event as a case study. Our objective is to provide measurement requirements and viable technology suggestions, through analysis of existing data and capabilities, to inform the development of future Surface Topography and Vegetation (STV) Earth observation system from the Solid Earth and earthquake hazard perspectives. This study uses satellite optical imagery and DEMs acquired by different satellite agencies and with different resolutions to measure ground surface displacements though sub-pixel cross-correlation of the orthorectified images (OIC). The main observations from this study are summarized as follows:

- Noise in the ground displacement maps increases linearly with decreasing optical imagery resolution, resulting in greater uncertainty in the measured displacement amplitudes across the fault zone.

- We infer an under-estimation of the measured displacements across the fault zone by a factor 0.7-0.8 when using low-resolution (>10 m) compared to high-resolution (≤1 m) imagery. This factor is independent of the processing method and has been inferred for multiple satellite observations on different earthquake case studies.

- The use of submeter-accuracy DEM/DSMs in both the pre- and post-earthquake periods allows for reducing topography related noise in the surface displacement products, and is necessary for assessing the earthquake vertical displacements through topography differencing.

- We suggest that high resolution (≤1 m) optical imagery and derived DSM products represents a preferred dataset for accurately measuring the ground displacements, both in the horizontal and vertical components, across active fault zones. Especially, the high resolution (≤1 m) is necessary to resolve complex fault geometries, as well as untangle the diffuse, distributed or localized nature of the surface deformation.
- High-resolution (<0.5 m) stereo optical imagery and associated photogrammetry and OIC techniques have a unique potential for 3-D analysis of the ground surface characteristics and change, and present themselves as a good candidate for the future STV Earth observation system from earthquake hazard perspectives and for other interdisciplinary applications areas such as volcanos and landslide monitoring, geomorphology and vegetation analysis, and cryosphere.

Acknowledgments

This work was carried out at the Jet Propulsion Laboratory, California Institute of Technology, under a contract with the National Aeronautics and Space Administration (80NM0018D0004), and supported by NASA Decadal Survey Incubator/Surface Topography and Vegetation program. Numerical computations were performed on the Gattaca/Gattaca-2 (JPL, USA) platform.

Open Research

MicMac (https://github.com/micmacIGN/micmac; last accessed on 01/03/24) and StackProf (https://github.com/IPGP/stackprof; last accessed on 01/03/24) are open source. WorldView and Planet data were accessed through the Commercial Smallsat Data Acquisition (CSDA) program of the National Aeronautics and Space Administration (https://www.earthdata.nasa.gov/esds/csda/commercial-datasets; last accessed on 01/03/24). Supplementary figures providing details on the methodology and on the results of this study, along with surface displacement maps and fault displacement and width measurements will be available for the published version of the manuscript.

References

Aati, S., Milliner, C., Avouac, J.-P., 2022. A new approach for 2-D and 3-D precise measurements of ground deformation from optimized registration and correlation of optical images and ICA-based filtering of image geometry artifacts. Remote Sensing of Environment 277, 113038. https://doi.org/10.1016/j.rse.2022.113038

Ajorlou, N., Hollingsworth, J., Mousavi, Z., Ghods, A., Masoumi, Z., 2021. Characterizing near-field surface deformation in the 1990 Rudbar earthquake (Iran) using optical image correlation. Geochemistry, Geophysics, Geosystems 22, 2021 009704. https://doi.org/10.1029/2021GC009704

Andreuttiova, L., Hollingsworth, J., Vermeesch, P., Mitchell, T.M., Bergman, E., 2022. Revisiting the 1959 Hebgen Lake Earthquake Using Optical Image Correlation; New Constraints on Near-Field 3D Ground Displacement. Geophysical Research Letters 49, e2022GL098666. https://doi.org/10.1029/2022GL098666

Antoine, S.L., Liu, Z., Delorme, A., Klinger, Y., 2024. Evidence of kilometer-wide shallow bulk plastic yielding along the 2021 Maduo, Tibet, surface rupture, and its relation with the dynamic rupture process (preprint). Preprints. https://doi.org/10.22541/essoar.170585943.30353472/v1

Antoine, S.L., Klinger, Y., Wang, K., Bürgmann, R., 2023. Diffuse deformation explains the magnitude-dependent coseismic shallow slip deficit (preprint). In Review. https://doi.org/10.21203/rs.3.rs-2536085/v1

Antoine, S.L., Klinger, Y., Delorme, A., Gold, R.D., 2022. Off-Fault Deformation in Regions of Complex Fault Geometries: The 2013, Mw7.7, Baluchistan Rupture (Pakistan). Journal of Geophysical Research: Solid Earth 127, e2022JB024480. https://doi.org/10.1029/2022JB024480

Antoine, S.L., Klinger, Y., Delorme, A., Wang, K., Bürgmann, R., Gold, R.D., 2021. Diffuse Deformation and Surface Faulting Distribution from Submetric Image Correlation along the 2019 Ridgecrest, California, Ruptures, in: Bulletin of the Seismological Society of America. https://doi.org/10.1785/0120210036

Avouac, J.-P., 2015. From Geodetic Imaging of Seismic and Aseismic Fault Slip to Dynamic Modeling of the Seismic Cycle. Annu. Rev. Earth Planet. Sci 43, 233–271. https://doi.org/10.1146/annurev-earth-060614-105302

Avouac, J.-P., Ayoub, F., Wei, S., Ampuero, J.-P., Meng, L., Leprince, S., Jolivet, R., Duputel, Z., Helmberger, D., 2014. The 2013, Mw 7.7 Balochistan earthquake, energetic strike-slip reactivation of a thrust fault. Earth Planet Sci Lett 391, 128–134. https://doi.org/10.1016/j.epsl.2014.01.036

Avouac, J.-P., Leprince, S., 2015. Geodetic Imaging Using Optical Systems, in: Treatise on Geophysics. Elsevier, pp. 387–424. https://doi.org/10.1016/B978-0-444-53802-4.00067-1

Ayoub, F., Leprince, S., Avouac, J.-P., 2009. Co-registration and correlation of aerial photographs for ground deformation measurements. ISPRS Journal of Photogrammetry and Remote Sensing 64, 551–560. https://doi.org/10.1016/j.isprsjprs.2009.03.005

Barnhart, W.D., Gold, R.D., Hollingsworth, J., 2020. Localized fault-zone dilatancy and surface inelasticity of the 2019 Ridgecrest earthquakes. Nature Geoscience 13, 699–704. https://doi.org/10.1038/s41561-020-0628-8

Barnhart, W.D., Gold, R.D., Shea, H.N., Peterson, K.E., Briggs, R.W., Harbor, D.J., 2019. Vertical Coseismic Offsets Derived From High-Resolution Stereogrammetric DSM Differencing: The 2013 Baluchistan, Pakistan Earthquake. Journal of Geophysical Research: Solid Earth 124, 6039–6055. https://doi.org/10.1029/2018JB017107

Bickel, V.T., Manconi, A., Amann, F., 2018. Quantitative Assessment of Digital Image Correlation Methods to Detect and Monitor Surface Displacements of Large Slope Instabilities. Remote Sensing 10, 865. https://doi.org/10.3390/rs10060865

Bontemps, N., Lacroix, P., Doin, M.-P., 2018. Inversion of deformation fields time-series from optical images, and application to the long term kinematics of slow-moving landslides in Peru. Remote Sensing of Environment 210, 144–158. https://doi.org/10.1016/j.rse.2018.02.023

Bornert, M., Brémand, F., Doumalin, P., Dupré, J.-C., Fazzini, M., Grédiac, M., Hild, F., Mistou, S., Molimard, J., Orteu, J.-J., Robert, L., Surrel, Y., Vacher, P., Wattrisse, B., 2009. Assessment of Digital Image Correlation Measurement Errors: Methodology and Results. Exp Mech 49, 353–370. https://doi.org/10.1007/s11340-008-9204-7

Bornert, M., Doumalin, P., Dupré, J.-C., Poilâne, C., Robert, L., Toussaint, E., Wattrisse, B., 2018. Assessment of Digital Image Correlation Measurement Accuracy in the Ultimate Error Regime: Improved Models of Systematic and Random Errors. Exp Mech 58, 33–48. https://doi.org/10.1007/s11340-017-0328-5

Borsa, A., Minster, J., 2012. Rapid Determination of Near-Fault Earthquake Deformation Using Differential LiDAR. Bulletin of the Seismological Society of America 102, 1335–1347. https://doi.org/10.1785/0120110159

Brosens, L., Campforts, B., Govers, G., Aldana-Jague, E., Razanamahandry, V.F., Razafimbelo, T., Rafolisy, T., Jacobs, L., 2022. Comparative analysis of the Copernicus, TanDEM-X, and UAV-SfM digital elevation models to estimate lavaka (gully) volumes and mobilization rates in the Lake Alaotra region (Madagascar). Earth Surface Dynamics 10, 209–227. https://doi.org/10.5194/esurf-10-209-2022

Chen, K., Avouac, J.-P., Aati, S., Milliner, C., Zheng, F., Shi, C., 2020. Cascading and pulse-like ruptures during the 2019 Ridgecrest earthquakes in the Eastern California Shear Zone. Nature Communications 11, 22. https://doi.org/10.1038/s41467-019-13750-w

Cheng, G., Barnhart, W.D., 2021. Permanent Co-Seismic Deformation of the 2013 Mw7.7 Baluchistan, Pakistan Earthquake From High-Resolution Surface Strain Analysis. Journal of Geophysical Research: Solid Earth 126, 2020 020622. https://doi.org/10.1029/2020JB020622

Cofaru, C., Philips, W., Paepegem, W.V., 2010. Improved Newton–Raphson digital image correlation method for full-field displacement and strain calculation. Appl. Opt., AO 49, 6472–6484. https://doi.org/10.1364/AO.49.006472

Dehecq, A., Gourmelen, N., Trouve, E., 2015. Deriving large-scale glacier velocities from a complete satellite archive: Application to the Pamir–Karakoram–Himalaya. Remote Sensing of Environment 162, 55–66. https://doi.org/10.1016/j.rse.2015.01.031

DeLong, S., Scott, C., Donnellan, A., Willard, J.G., Hammer, M., Powell, J.H., Arrowsmith, R., 2022. Remote Sensing of Fault Slip, Fault Creep, and Landscape Change: Implications for Surface Topography and Vegetation Measurement Needs. 2022, GC15F-02.

Delorme, A., Grandin, R., Klinger, Y., Pierrot-Deseilligny, M., Feuillet, N., Jacques, E., Rupnik, E., Morishita, Y., 2020b. Complex Deformation at Shallow Depth During the 30 October 2016 Mw6.5 Norcia Earthquake: Interference Between Tectonic and Gravity Processes? Tectonics 39, 2019 005596. https://doi.org/10.1029/2019TC005596

Delouis, B., Ende, M.V.D., Ampuero, J.-P., 2023. Kinematic rupture model of the February 6th 2023 Mw7.8 Turkey earthquake from a large set of near-source strong motion records combined by GNSS offsets reveals intermittent supershear rupture (preprint). Preprints. https://doi.org/10.22541/essoar.168286647.71550161/v1

Dematteis, N., Giordan, D., 2021. Comparison of Digital Image Correlation Methods and the Impact of Noise in Geoscience Applications. Remote Sensing 13, 327. https://doi.org/10.3390/rs13020327

Donnellan, A., 2021. Observing Earths Surface Topography and Vegetation Structure in the Next Decade: Science Objectives and Needs 2021, U32A-01.

Donnellan, A., Arrowsmith, R., DeLong, S., 2017. Spatio-Temporal Mapping of Plate Boundary Faults in California Using Geodetic Imaging. Geosciences 7, 15. https://doi.org/10.3390/geosciences7010015

Donnellan, A., Padgett, C., Green, J.J., Zinke, R.W., Arrowsmith, R., DeLong, S., 2022. QUAKES-I Airborne Spatial and Temporal Topography and Analysis for Achieving Surface Topography and Vegetation (STV) Goals. Presented at the Fall Meeting 2022, AGU.

DuRoss, C.B., Gold, R.D., Dawson, T.E., Scharer, K.M., Kendrick, K.J., Akciz, S.O., Angster, S.J., Bachhuber, J., Bacon, S., Bennett, S.E.K., Blair, L., Brooks, B.A., Bullard, T., Burgess, W.P., Chupik, C., DeFrisco, M., Delano, J., Dolan, J.F., Frost, E., Graehl, N., Haddon, E.K., Hatem, A.E., Hernandez, J.L., Hitchcock, C., Hudnut, K., Jobe, J.T., Koehler, R., Kozaci, O., Ladinsky, T., Madugo, C., McPhillips, D.S., Milliner, C., Morelan, A., Olson, B., Patton, J., Philibosian, B., Pickering, A.J., Pierce, I., Ponti, D.J., Seitz, G., Spangler, E., Swanson, B., Thomas, K., Treiman, J., Valencia, F., Williams, A., Zinke, R., 2020. Surface Displacement Distributions for the. Bulletin of the Seismological Society of America 110, 1400–1418. https://doi.org/10.1785/0120200058

Fan, X., Zhang, G., Zhao, D., Xie, C., Huang, C., Shan, X., 2022. Fault geometry and kinematics of the 2021 Mw 7.3 Maduo earthquake from aftershocks and InSAR observations. Frontiers in Earth Science 10, 993984. https://doi.org/10.3389/feart.2022.993984

Fialko, Y., Sandwell, D., Simons, M., Rosen, P., 2005. Three-dimensional deformation caused by the Bam, Iran, earthquake and the origin of shallow slip deficit. Nature 435, 295–299. https://doi.org/10.1038/nature03425

Fialko, Y., Simons, M., Agnew, D., 2001. The complete (3-D) surface displacement field in the epicentral area of the 1999 MW7.1 Hector Mine earthquake, California, from space geodetic observations. Geophys. Res. Lett 28, 3063–3066. https://doi.org/10.1029/2001GL013174

Fielding, E.J., Liu, Z., Stephenson, O.L., Zhong, M., Liang, C., Moore, A., Yun, S.-H., Simons, M., 2020. Surface deformation related to the 2019 Mw 7.1 and 6.4 Ridgecrest earthquakes in California from GPS, SAR interferometry, and SAR pixel offsets. Seismol. Res. Lett 91, 2035–2046. https://doi.org/10.1785/0220190302

Fielding, E.J., Sladen, A., Li, Z., Avouac, J.-P., Bürgmann, R., Ryder, I., 2013. Kinematic fault slip evolution source models of the 2008 M7.9 Wenchuan earthquake in China from SAR interferometry, GPS and teleseismic analysis and implications for Longmen Shan tectonics. Geophysical Journal International 194, 1138–1166. https://doi.org/10.1093/gji/ggt155

Florinsky, I.V., Skrypitsyna, T.N., Luschikova, O.S., 2018. Comparative accuracy of the AW3D30 DSM, ASTER GDEM, and SRTM1 DEM: A case study on the Zaoksky testing ground, Central European Russia. Remote Sensing Letters 9, 706–714. https://doi.org/10.1080/2150704X.2018.1468098

Floyd, M., Funning, G., Fialko, Y., Terry, R., Herring, T., 2020. Survey and continuous GNSS in the vicinity of the July 2019 Ridgecrest earthquakes. Seismol. Res. Lett 91, 2047–2054. https://doi.org/10.1785/0220190324

García Aranda, J.J., Alarcón Granero, M., Juan Quintanilla, F.J., Caffarena, G., García-Carmona, R., 2021. Elastic Downsampling: An Adaptive Downsampling Technique to Preserve Image Quality. Electronics 10, 400. https://doi.org/10.3390/electronics10040400

Gold, R.D., DuRoss, C.B., Barnhart, W.D., 2021. Coseismic surface displacement in the 2019 Ridgecrest earthquakes: Comparison of field measurements and optical image correlation results. Geochem. Geophys. Geosystems 22, 2020 009326. https://doi.org/10.1029/2020GC009326

Gold, R.D., Reitman, N.G., Briggs, R.W., Barnhart, W.D., Hayes, G.P., Wilson, E., 2015. Onand off-fault deformation associated with the September 2013 Mw 7.7 Balochistan earthquake: Implications for geologic slip rate measurements. Tectonophysics 660, 65–78. https://doi.org/10.1016/j.tecto.2015.08.019

Hasegawa, H., Matsuo, K., Koarai, M., Watanabe, N., Masaharu, H., Fukushima, Y., 2000. DEM accuracy and the base to height (B/H) ratio of stereo images. International Archives of Photogrammetry and Remote Sensing 33.

He, K., Wen, Y., Xu, C., Zhao, Y., 2021. Fault Geometry and Slip Distribution of the 2021 Mw 7.4 Maduo, China, Earthquake Inferred from InSAR Measurements and Relocated Aftershocks. Seismological Research Letters 93, 8–20. https://doi.org/10.1785/0220210204

He, L., Feng, G., Wu, X., Lu, H., Xu, W., Wang, Y., Liu, J., Hu, J., Li, Z., 2021. Coseismic and Early Postseismic Slip Models of the 2021 Mw 7.4 Maduo Earthquake (Western China) Estimated by Space-Based Geodetic Data. Geophysical Research Letters 48, e2021GL095860. https://doi.org/10.1029/2021GL095860

He, L., Feng, G., Xu, W., Wang, Y., Xiong, Z., Gao, H., Liu, X., 2023. Coseismic Kinematics of the 2023 Kahramanmaras, Turkey Earthquake Sequence From InSAR and Optical Data. Geophysical Research Letters 50, e2023GL104693. https://doi.org/10.1029/2023GL104693

Hu, F., Gao, X.M., Li, G.Y., Li, M., 2016. DEM EXTRACTION FROM WORLDVIEW-3 STEREO-IMAGES AND ACCURACY EVALUATION. Int. Arch. Photogramm. Remote Sens. Spatial Inf. Sci. XLI-B1, 327–332. https://doi.org/10.5194/isprsarchives-XLI-B1-327-2016

Jin, Z., Fialko, Y., 2021. Coseismic and Early Postseismic Deformation Due to the 2021 M7.4 Maduo (China) Earthquake. Geophysical Research Letters 48. https://doi.org/10.1029/2021GL095213

Jolivet, R., Duputel, Z., Riel, B., Simons, M., Rivera, L., Minson, S.E., Zhang, H., Aivazis, M., Ayoub, F., Leprince, S., Samsonov, S., Motagh, M., Fielding, E., 2014. The 2013 Mw7.7 Balochistan earthquake: Seismic potential of an accretionary wedge. Bulletin of the Seismological Society of America 104, 1020–1030. https://doi.org/10.1785/0120130313

Klinger, Y., Xu, X., Tapponnier, P., Woerd, J., Lasserre, C., King, G., 2005. High-resolution satellite imagery mapping of the surface rupture and slip distribution of the Mw 7.8, Kokoxili earthquake, Kunlun fault, northern Tibet, China.

Lauer, B., Grandin, R., Klinger, Y., 2020. Fault geometry and slip distribution of the 2013 Mw 7.7 Balochistan earthquake from inversions of SAR and optical data. J. Geophys. Res. Solid Earth 125, 2019 018380. https://doi.org/10.1029/2019JB018380

Leprince, S., Barbot, S., Ayoub, F., Avouac, J.-P., 2007. Automatic and Precise Orthorectification, Coregistration, and Subpixel Correlation of Satellite Images, Application to Ground Deformation Measurements. Geoscience and Remote Sensing, IEEE Transactions on 45, 1529–1558. https://doi.org/10.1109/TGRS.2006.888937

Li, C., Li, T., Hollingsworth, J., Zhang, Y., Qian, L., Shan, X., 2023. Strain Threshold for the Formation of Coseismic Surface Rupture. Geophysical Research Letters 50, e2023GL103666. https://doi.org/10.1029/2023GL103666

Li, C., Li, T., Shan, X., Zhang, G., 2022. Extremely Large Off-Fault Deformation during the 2021 Mw 7.4 Maduo, Tibetan Plateau, Earthquake. Seismological Research Letters. https://doi.org/10.1785/0220220139

Li, Q., Wan, Y., Li, C., Tang, H., Tan, K., Wang, D., 2022. Source Process Featuring Asymmetric Rupture Velocities of the 2021 Mw 7.4 Maduo, China, Earthquake from Teleseismic and Geodetic Data. Seismological Research Letters 93, 1429–1439. https://doi.org/10.1785/0220210300

Liu, C., Bai, L., Hong, S., Dong, Y., Jiang, Y., Li, H., Zhan, H., Chen, Z., 2021. Coseismic deformation of the 2021 *M*w7.4 Maduo earthquake from joint inversion of InSAR, GPS, and teleseismic data. dzxbywb 34, 436–446. https://doi.org/10.29382/eqs-2021-0050

Liu, J., Hu, J., Li, Z., Ma, Z., Wu, L., Jiang, W., Feng, G., Zhu, J., 2022. Complete three-dimensional coseismic displacements due to the 2021 Maduo earthquake in Qinghai Province, China from Sentinel-1 and ALOS-2 SAR images. Sci. China Earth Sci. 65, 687–697. https://doi.org/10.1007/s11430-021-9868-9

Loghin, A.-M., Otepka-Schremmer, J., Pfeifer, N., 2020. Potential of Pléiades and WorldView-3 Tri-Stereo DSMs to Represent Heights of Small Isolated Objects. Sensors 20, 2695. https://doi.org/10.3390/s20092695

Marchandon, M., Hollingsworth, J., Radiguet, M., 2021. Origin of the shallow slip deficit on a strike slip fault: Influence of elastic structure, topography, data coverage, and noise. Earth and Planetary Science Letters 554, 116696. https://doi.org/10.1016/j.epsl.2020.116696

Massonnet, D., Rossi, M., Carmona, C., Adragna, F., Peltzer, G., Feigl, K., Rabaute, T., 1993. The displacement field of the Landers earthquake mapped by radar interferometry. Nature 364, 138–142. https://doi.org/10.1038/364138a0

Milliner, C., Donnellan, A., 2020. Using Planet Labs satellite imagery to separate the surface deformation between the July 4th Mw 6.4 foreshock and July 5th Mw 7.1 mainshock during the 2019 Ridgecrest earthquake sequence. Seismol. Res. Lett 91, 1986–1997. https://doi.org/10.1785/0220190271

Milliner, C., Donnellan, A., Aati, S., Avouac, J.-P., Zinke, R., Dolan, J.F., Wang, K., Bürgmann, R., 2021. Bookshelf kinematics and the effect of dilatation on fault zone inelastic deformation: Examples from optical image correlation measurements of the 2019 Ridgecrest earthquake sequence. J. Geophys. Res. Solid Earth 126, 2020 020551. https://doi.org/10.1029/2020JB020551

Milliner, C.W.D., Aati, S., Avouac, J.P., 2022. Fault Friction Derived From Fault Bend Influence on Coseismic Slip During the 2019 Ridgecrest Mw 7.1 Mainshock. Journal of Geophysical Research: Solid Earth 127, e2022JB024519. https://doi.org/10.1029/2022JB024519

Milliner, C.W.D., Dolan, J.F., Hollingsworth, J., Leprince, S., Ayoub, F., 2016. Comparison of coseismic near-field and off-fault surface deformation patterns of the 1992 Mw 7.3 Landers and 1999 Mw 7.1 Hector Mine earthquakes: Implications for controls on the distribution of surface strain. Geophys. Res. Lett 43, 10,115-10,124. https://doi.org/10.1002/2016GL069841

Montagnon, T., Hollingsworth, J., Pathier, E., Marchandon, M., Mura, M.D., Giffard-Roisin, S., 2023. A New Deep-Learning Approach for the Sub-Pixel Registration of Satellite Images Containing Sharp Displacement Discontinuities, in: IGARSS 2023 - 2023 IEEE International Geoscience and Remote Sensing Symposium. Presented at the IGARSS 2023 - 2023 IEEE International Geoscience and Remote Sensing Symposium, pp. 5123–5126. https://doi.org/10.1109/IGARSS52108.2023.10283255

Nissen, E., Maruyama, T., Ramon Arrowsmith, J., Elliott, J.R., Krishnan, A.K., Oskin, M.E., Saripalli, S., 2014. Coseismic fault zone deformation revealed with differential lidar: Examples from Japanese Mw ~7 intraplate earthquakes. Earth and Planetary Science Letters 405, 244–256. https://doi.org/10.1016/j.epsl.2014.08.031

Pan, J., Li, H., Chevalier, M.-L., Tapponnier, P., Bai, M., Li, Chao, Liu, F., Liu, D., Wu, K., Wang, P., Li, Chunrui, Lu, H., Chen, P., 2022. Co-seismic rupture of the 2021, Mw7.4 Maduo earthquake (northern Tibet): Short-cutting of the Kunlun fault big bend. Earth and Planetary Science Letters 594, 117703. https://doi.org/10.1016/j.epsl.2022.117703

Puymbroeck, N.V., Michel, R., Binet, R., Avouac, J.-P., Taboury, J., 2000. Measuring earthquakes from optical satellite images. Appl. Opt., AO 39, 3486–3494. https://doi.org/10.1364/AO.39.003486

Ragon, T., Simons, M., 2020. Accounting for uncertain 3-D elastic structure in fault slip estimates. Geophysical Journal International 224, 1404–1421. https://doi.org/10.1093/gji/ggaa526

Reitman, N.G., Briggs, R.W., Barnhart, W.D., Hatem, A.E., Thompson Jobe, J.A., DuRoss, C.B., Gold, R.D., Mejstrik, J.D., Collett, C., Koehler, R.D., Akçiz, S., 2023. Rapid Surface Rupture Mapping from Satellite Data: The 2023 Kahramanmaraş, Turkey (Türkiye), Earthquake Sequence. The Seismic Record 3, 289–298. https://doi.org/10.1785/0320230029

Reitman, N.G., Mueller, K.J., Tucker, G.E., 2022. Surface slip variability on strike-slip faults. Earth Surf Processes Landf 47, 908–935. https://doi.org/10.1002/esp.5294

Ren, J., Xu, X., Zhang, G., Wang, Q., Zhang, Z., Gai, H., Kang, W., 2022. Coseismic surface ruptures, slip distribution, and 3D seismogenic fault for the 2021 Mw 7.3 Maduo earthquake, central Tibetan Plateau, and its tectonic implications. Tectonophysics 827, 229275. https://doi.org/10.1016/j.tecto.2022.229275

Ren, J., Zhang, Z., Gai, H., Kang, W., 2021. Typical Riedel shear structures of the coseismic surface rupture zone produced by the 2021 Mw 7.3 Maduo earthquake, Qinghai, China, and the implications for seismic hazards in the block interior. Natural Hazards Research 1, 145–152. https://doi.org/10.1016/j.nhres.2021.10.001

Rockwell, T., Lindvall, S., Dawson, T., Langridge, R., Lettis, W., Klinger, Y., 2002. Lateral Offsets on Surveyed Cultural Features Resulting from the 1999 Izmit and Düzce Earthquakes, Turkey. Bulletin of the Seismological Society of America 92, 79–94. https://doi.org/10.1785/0120000809

Rosu, A.-M., Pierrot-Deseilligny, M., Delorme, A., Binet, R., Klinger, Y., 2015c. Measurement of ground displacement from optical satellite image correlation using the free open-source software MicMac. ISPRS J. Photogramm. Remote Sens., High-Resolution Earth Imaging for Geospatial Information 100, 48–59. https://doi.org/10.1016/j.isprsjprs.2014.03.002

Rupnik, E., Daakir, M., Pierrot Deseilligny, M., 2017. MicMac – a free, open-source solution for photogrammetry. Open Geospatial Data Softw. Stand 2, 14. https://doi.org/10.1186/s40965-017-0027-2

Rupnik, E., Deseilligny, M.P., Delorme, A., Klinger, Y., 2016. Refined satellite image orientation in the free open-source photogrammetric tools Apero/MicMac. ISPRS Ann. Photogramm. Remote Sens 3, 83–90. https://doi.org/10.5194/isprsannals-III-1-83-2016

Rupnik, E., Pierrot-Deseilligny, M., Delorme, A., 2018. 3D reconstruction from multi-view VHR-satellite images in MicMac. ISPRS J. Photogramm. Remote Sens 139, 201–211. https://doi.org/10.1016/j.isprsjprs.2018.03.016

Schumann, G.J.-P., Bates, P.D., 2018. The Need for a High-Accuracy, Open-Access Global DEM. Frontiers in Earth Science 6.

Scott, C.P., Arrowsmith, J.R., Nissen, E., Lajoie, L., Maruyama, T., Chiba, T., 2018. The M7 2016 Kumamoto, Japan, Earthquake: 3-D Deformation Along the Fault and Within the Damage Zone Constrained From Differential Lidar Topography. Journal of Geophysical Research: Solid Earth 123, 6138–6155. https://doi.org/10.1029/2018JB015581

Scott, C.P., DeLong, S.B., Arrowsmith, J.R., 2020. Distribution of Aseismic Deformation Along the Central San Andreas and Calaveras Faults From Differencing Repeat Airborne Lidar. Geophysical Research Letters 47, e2020GL090628. https://doi.org/10.1029/2020GL090628

Segall, P., 2010. Earthquake and Volcano Deformation, STU-Student. ed. Princeton University Press.

Shean, D.E., Alexandrov, O., Moratto, Z.M., Smith, B.E., Joughin, I.R., Porter, C., Morin, P., 2016. An automated, open-source pipeline for mass production of digital elevation models (DEMs) from very-high-resolution commercial stereo satellite imagery. ISPRS Journal of Photogrammetry and Remote Sensing 116, 101–117. https://doi.org/10.1016/j.isprsjprs.2016.03.012

Shean, D.E., Bhushan, S., Montesano, P., Rounce, D.R., Arendt, A., Osmanoglu, B., 2020. A Systematic, Regional Assessment of High Mountain Asia Glacier Mass Balance. Frontiers in Earth Science 7.

Simons, M., Fialko, Y., Rivera, L., 2002. Coseismic Deformation from the 1999 M_w 7.1 Hector Mine, California, Earthquake as Inferred from InSAR and GPS Observations. Bulletin of the Seismological Society of America 92, 1390–1402.

Socquet, A., Hollingsworth, J., Pathier, E., Bouchon, M., 2019. Evidence of supershear during the 2018 magnitude 7.5 Palu earthquake from space geodesy. Nat. Geosci 12, 192–199. https://doi.org/10.1038/s41561-018-0296-0

Stumpf, A., Michéa, D., Malet, J.-P., 2018. Improved Co-Registration of Sentinel-2 and Landsat-8 Imagery for Earth Surface Motion Measurements. Remote Sensing 10, 160. https://doi.org/10.3390/rs10020160

Su, Y., Zhang, Q., 2016. Random errors in DIC caused by non-uniform image noise, in: Optical Measurement Technology and Instrumentation. Presented at the Optical Measurement Technology and Instrumentation, SPIE, pp. 16–21. https://doi.org/10.1117/12.2243571

Teran, O.J., 2015. Geologic and structural controls on rupture zone fabric: A field-based study of the 2010 Mw 7.2 El Mayor–Cucapah earthquake surface rupture. Geosphere 11, 899–920.

Teran, O.J., Fletcher, J.M., Oskin, M.E., Rockwell, T.K., Hudnut, K.W., Spelz, R.M., Akciz, S.O., Hernandez-Flores, A.P., Morelan, A.E., 2015. Geologic and structural controls on rupture zone fabric: A field-based study of the 2010 Mw 7.2 El Mayor–Cucapah earthquake surface rupture. Geosphere 11, 899–920. https://doi.org/10.1130/GES01078.1

Tong, X., Sandwell, D.T., Fialko, Y., 2010. Coseismic slip model of the 2008 Wenchuan earthquake derived from joint inversion of interferometric synthetic aperture radar, GPS, and field data. Journal of Geophysical Research: Solid Earth 115.

Tong, X., Xu, X., Chen, S., 2022. Coseismic Slip Model of the 2021 Maduo Earthquake, China from Sentinel-1 InSAR Observation. Remote Sensing 14, 436. https://doi.org/10.3390/rs14030436

Uuemaa, E., Ahi, S., Montibeller, B., Muru, M., Kmoch, A., 2020. Vertical Accuracy of Freely Available Global Digital Elevation Models (ASTER, AW3D30, MERIT, TanDEM-X, SRTM, and NASADEM). Remote Sensing 12, 3482. https://doi.org/10.3390/rs12213482

Vallage, A., Klinger, Y., Grandin, R., Bhat, H.S., Pierrot-Deseilligny, M., 2015. Inelastic surface deformation during the 2013 Mw 7.7 Balochistan, Pakistan, earthquake. Geology 43, 1079–1082. https://doi.org/10.1130/G37290.1

Wang, K., Dreger, D., Tinti, E., Burgmann, R., Taira, T., 2020. Rupture Process of the 2019 Ridgecrest, California Mw 6.4 Foreshock and Mw 7.1 Earthquake Constrained by Seismic and Geodetic Data, in: Bulletin of the Seismological Society of America. https://doi.org/10.1785/0120200108

Wang, K., Fialko, Y., 2015. Slip model of the 2015 Mw 7.8 Gorkha (Nepal) earthquake from inversions of ALOS-2 and GPS data. Geophysical Research Letters 42, 7452–7458. https://doi.org/10.1002/2015GL065201

Wang, S., Ren, Z., Wu, C., Lei, Q., Gong, W., Ou, Q., Zhang, H., Ren, G., Li, C., 2019. DEM generation from Worldview-2 stereo imagery and vertical accuracy assessment for its application in active tectonics. Geomorphology 336, 107–118. https://doi.org/10.1016/j.geomorph.2019.03.016

Wei, S., Zeng, H., Shi, Q., Liu, J., Luo, H., Hu, W., Li, Y., Wang, W., Ma, Z., Liu-Zeng, J., Wang, T., 2022. Simultaneous Rupture Propagation Through Fault Bifurcation of the 2021 Mw7.4 Maduo Earthquake. Geophysical Research Letters 49, e2022GL100283. https://doi.org/10.1029/2022GL100283

Willis, M.J., Barnhart, W.D., Cassotto, R., Klassen, J., Corcoran, J., Host, T., Huberty, B., Pelletier, K., Knight, J.F., 2019. CaliDEM: Ridgecrest, CA region 2m digital surface elevation model, in: Funding by NSF and USGS. Data Collection by DigitalGlobe. Distributed by OpenTopography. https://doi.org/10.5069/G998854C

Xie, H., Li, Z., Yuan, D., Wang, X., Su, Q., Li, X., Wang, A., Su, P., 2022. Characteristics of Co-Seismic Surface Rupture of the 2021 Maduo Mw 7.4 Earthquake and Its Tectonic Implications for Northern Qinghai–Tibet Plateau. Remote Sensing 14, 4154. https://doi.org/10.3390/rs14174154

Xiong, W., Chen, W., Wang, D., Wen, Y., Nie, Z., Gang, L., Dijin, W., Yu, P., Qiao, X., Zhao, B., 2022. Coseismic slip and early afterslip of the 2021 Mw 7.4 Maduo, China earthquake constrained by GPS and InSAR data. Tectonophysics 840, 229558. https://doi.org/10.1016/j.tecto.2022.229558

Xu, X., Tong, X., Sandwell, D.T., Milliner, C.W.D., Dolan, J.F., Hollingsworth, J., Leprince, S., Ayoub, F., 2016. Refining the shallow slip deficit. Geophys. J. Int 204, 1843–1862. https://doi.org/10.1093/gji/ggv563

Yang, Y.-H., Xu, Q., Hu, J.-C., Wang, Y.-S., Dong, X.-J., Chen, Q., Zhang, Y.-J., Li, H.-L., 2022. Source Model and Triggered Aseismic Faulting of the 2021 Mw 7.3 Maduo Earthquake Revealed by the UAV-Lidar/Photogrammetry, InSAR, and Field Investigation. Remote Sensing 14, 5859. https://doi.org/10.3390/rs14225859

Yin, T., Montesano, P.M., Cook, B.D., Chavanon, E., Neigh, C.S.R., Shean, D., Peng, D., Lauret, N., Mkaouar, A., Regaieg, O., Zhen, Z., Qin, R., Gastellu-Etchegorry, J.-P., Morton, D.C., 2023. Modeling forest canopy surface retrievals using very high-resolution spaceborne stereogrammetry: (II) optimizing acquisition configurations. Remote Sensing of Environment 298, 113824. https://doi.org/10.1016/j.rse.2023.113824

Yuan, Z., Li, T., Su, P., Sun, H., Ha, G., Guo, P., Chen, G., Jobe, J., 2022. Large Surface-Rupture Gaps and Low Surface Fault Slip of the 2021 Mw 7.4 Maduo Earthquake Along a Low-Activity Strike-Slip Fault, Tibetan Plateau. Geophysical Research Letters 49. https://doi.org/10.1029/2021GL096874

Zhang, X., Feng, W., Du, H., Samsonov, S., Yi, L., 2022. Supershear Rupture During the 2021 MW 7.4 Maduo, China, Earthquake. Geophysical Research Letters 49, e2022GL097984. https://doi.org/10.1029/2022GL097984

Zhao, D., Qu, C., Chen, H., Shan, X., Song, X., Gong, W., 2021. Tectonic and Geometric Control on Fault Kinematics of the 2021 Mw7.3 Maduo (China) Earthquake Inferred From Interseismic, Coseismic, and Postseismic InSAR Observations. Geophysical Research Letters 48. https://doi.org/10.1029/2021GL095417

Zhou, Y., Parsons, B., Elliott, J.R., Barisin, I., Walker, R.T., 2015. Assessing the ability of Pleiades stereo imagery to determine height changes in earthquakes: A case study for the El Mayor-Cucapah epicentral area. Journal of Geophysical Research: Solid Earth 120, 8793–8808. https://doi.org/10.1002/2015JB012358

Zhou, Y., Parsons, B.E., Walker, R.T., 2018. Characterizing complex surface ruptures in the 2013 Mw 7.7 Balochistan earthquake using three-dimensional displacements. J. Geophys. Res. Solid Earth 123, 10191–10211. https://doi.org/10.1029/2018JB016043

Zinke, R., Hollingsworth, J., Dolan, J.F., 2014. Surface slip and off-fault deformation patterns in the 2013 MW 7.7 Balochistan, Pakistan earthquake: Implications for controls on the distribution of near-surface coseismic slip. Geochem. Geophys. Geosystems 15, 5034–5050. https://doi.org/10.1002/2014GC005538

Zinke, R., Hollingsworth, J., Dolan, J.F., Dissen, R.V., 2019. Three-dimensional surface deformation in the 2016 MW 7.8 Kaikōura, New Zealand, earthquake from optical image correlation: Implications for strain localization and long-term evolution of the Pacific-Australian plate boundary. Geochem. Geophys. Geosystems 20, 1609–1628. https://doi.org/10.1029/2018GC007951